

## Disturbed cold gas in galaxy and structure formation

Siwei Zou<sup>1\*</sup>, Robert A. Simcoe<sup>2</sup>, Patrick Petitjean<sup>3</sup>, Céline Péroux<sup>4,5</sup>, Jaclyn B. Champagne<sup>6</sup>, Feige Wang<sup>6</sup>, Jinning Liang<sup>7</sup>, Fangzhou Jiang<sup>7</sup>, Zihao Li<sup>8,9</sup>, Wen Sun<sup>7</sup>, Xiaohui Fan<sup>6</sup>, Jinyi Yang<sup>6</sup>, Luis C. Ho<sup>7</sup>, Xiaojing Lin<sup>10,6</sup>, Jianan Li<sup>10</sup>, Jianwei Lyu<sup>6</sup>, Lile Wang<sup>7</sup>, Weizhe Liu<sup>6</sup>, Emanuele Paolo Farina<sup>11</sup>, Xiangyu Jin<sup>6</sup>, Cheng Cheng<sup>1</sup>

<sup>1</sup>Chinese Academy of Sciences South America Center for Astronomy, National Astronomical Observatories, CAS, Beijing 100101, China

<sup>2</sup>MIT Kavli Institute for Astrophysics and Space Research, 77 Massachusetts Avenue, Cambridge, MA 02139, USA

<sup>3</sup>Institut d'Astrophysique de Paris 98bis Boulevard Arago, 75014, Paris, France

<sup>4</sup>European Southern Observatory, Karl-Schwarzschild-Str. 2, 85748 Garching near Munich, Germany

<sup>5</sup>Aix Marseille Univ., CNRS, LAM, (Laboratoire d'Astrophysique de Marseille), UMR 7326, F-13388 Marseille, France

<sup>6</sup>Steward Observatory, University of Arizona, 933 N Cherry Avenue, Tucson, AZ 85721, USA

<sup>7</sup>Kavli Institute for Astronomy and Astrophysics, Peking University, Beijing 100871, China

<sup>8</sup>Cosmic Dawn Center (DAWN), Denmark

<sup>9</sup>Niels Bohr Institute, University of Copenhagen, Jagtvej 128, DK-2200, Copenhagen N, Denmark

<sup>10</sup>Department of Astronomy, Tsinghua University, Beijing 100084, China

<sup>11</sup>Gemini Observatory, NSF's NOIRLab, 670 N A'ohoku Place, Hilo, HI 96720, USA

**Cold and cool gas ( $T \leq 10^4$  K) in the circumgalactic medium (CGM) and its interaction with galaxies remain poorly understood. Simulations predict that cold gas flows into galaxies through cosmic filaments, determining the disk formation and galaxy evolution. The cold gas accretion modes in the CGM and their dependence on dark matter halo mass and redshift remain puzzling. Resolving the kiloparsec-scale kinematics and dynamics of cold gas interacting with the disk, dust, and metals in different environments is particularly lacking at  $z > 2$ . Here we report two disturbed cold gas structures traced by ultra-strong Mg II absorbers (rest-frame equivalent width  $W_r > 2 \text{ \AA}$ ) exhibiting high kinematic velocities ( $> 500 \text{ km s}^{-1}$ ) and their environments at  $z \sim 4.9$  and  $z \sim 2.6$ . Observations were conducted with VLT/MUSE, JWST/NIRCam, and ALMA to detect**

**Ly $\alpha$  and nebular emission lines, as well as dust continuum emission in the vicinity of these two absorbing gas structures. We identify two Ly $\alpha$  emitters associated with a strong Mg II absorber pair separated by  $\sim 1000 \text{ km s}^{-1}$  at  $z \sim 4.87$ . The pair exhibits relative differences in metallicity, dust content, and ionization states, suggesting internal metal and dust exchange within the ultra-large cold gas structure. For the strong Mg II absorber at  $z = 2.5652$ , we detect a dusty star-forming galaxy at a projected distance of  $D = 38 \text{ kpc}$ . This galaxy exhibits prominent He I, [S III], and Paschen $\gamma$  lines, along with significant dust continuum. It has a star formation rate of  $\sim 121 \pm 33 M_{\odot}/\text{yr}$  and likely harbors a rotating disk. These findings tentatively suggest that cold gas at high redshifts plays a critical role in driving disk formation and actively participates in the transfer of metals and dust within the overdense regions of the CGM.**

Cold gas plays a key role in galaxy formation and structural evolution<sup>1</sup>. The Mg II doublet ( $\lambda\lambda 2796, 2803$ ) absorption is ubiquitously observed in the gaseous halos in and around galaxies and is associated with cool ( $T \sim 10^4$  K) gas. Strong Mg II (rest-frame equivalent width  $W_r > 0.3 \text{ \AA}$ ) is detected in connection optically-thick neutral hydrogen gas ( $10^{16.0} < N(\text{H I}) < 10^{22.0} \text{ cm}^{-2}$ ) and, consequently, with star forming activities<sup>2</sup>. The evolution of strong Mg II absorbers is consistent with the trend of the global cosmic star formation rate at  $2 < z < 6$ <sup>3-5</sup>. Strong Mg II systems are detected in association with star-forming galaxies<sup>6-9</sup> and metal-enriched overdense regions<sup>9-12</sup>.

The ultra-strong Mg II systems (hereafter USMGII,  $W_r > 3 \text{ \AA}$ ) can trace cold and dense gas, and their origin remains uncertain. Kinematically broad Mg II systems have been observed to be associated with highly disturbed cold (and even molecular) gas<sup>13</sup>. Two primary scenarios have been proposed to explain the origin of USMGII absorbers: (a) they may arise from starburst-driven outflows or tidally stripped gas resulting from a major interaction<sup>14</sup>. In this scenario, the  $W_r$  and velocity spread ( $\Delta v$ ) of the gas are correlated with the star formation rate (SFR) and luminosity of the host galaxy<sup>15</sup>. (b) multiple 'normal' galaxies within a galaxy group could

\*E-mail: siwei1905@gmail.com

contribute to the strong absorption strength and kinematics observed<sup>15–17</sup>. Both scenarios have observational support at  $z < 1$ . USMGII systems at  $z < 1$  are detected at low impact parameters of bright galaxies<sup>18,19</sup>, supporting the outflow model. Meanwhile, a USMg II system at  $z \sim 0.5$  has been found to be associated with three galaxies within 200 kpc, suggesting the possibility of the galaxy group scenario<sup>20</sup>. It is also plausible that these two mechanisms coexist.

The connection between the metallicity and kinematics in the multiphase circumgalactic medium (CGM) and surrounding environments have been investigated in several observatory-based MUSE, ALMA, and JWST surveys. The MUSE-ALMA Haloes Survey<sup>21</sup> combined data from VLT/MUSE, ALMA, and HST to investigate strong H I and metal-absorbing gas at  $0.3 < z < 1.4$ . The study revealed that damped Ly $\alpha$  systems (DLAs,  $\log N(\text{H I}) > 20.3$ ) with strong Mg II absorption at  $z < 1$  are associated with multiple star-forming galaxies. The kinematics of the absorbing gas are linked to the ionized and molecular gas in the surrounding galaxies<sup>22–24</sup>. The MusE GAs FLOW and Wind (MEGAFLOW) survey has identified a bimodal relationship between the azimuthal angle and metallicity of cool gas at  $z \sim 1$ , suggesting that Mg II gas traces either galactic inflow<sup>25</sup> or galactic outflow<sup>26</sup>. The MUSE Analysis of Gas around Galaxies (MAGG) survey investigates the connection between [O II] emission and Mg II absorbers at  $z \sim 1$ <sup>27</sup>, as well as the connection between Ly $\alpha$  emission and C IV and Si IV absorbers at  $z = 3–4.5$ <sup>28,29</sup>. They found that the strength and kinematics of metal-enriched absorbing gas positively correlate with the number of Ly $\alpha$  emitters (LAEs). Furthermore, ALMA observations indicate that DLA systems at  $z \sim 4$  are associated with [C II] emission in disk galaxies<sup>30,31</sup>. Recent JWST observations have identified additional nebular emission lines, including H $\alpha$ , [O III], and H $\beta$  near Mg II absorbers at  $z = 2–7$ <sup>11,12,32,33</sup>. However, the majority of Mg II absorbers are not classified as very strong Mg II systems, indicating that the traced gas is more likely associated with warm gas.

To study the disturbed cold gas in the CGM and its interaction with galaxies and large-scale structures at  $z > 2$ , we conducted an initial survey. To date, no dedicated survey has focused on studying the galaxy environments around very strong and kinematically broad Mg II absorbers at  $z > 2$ . We use JWST/NIRCam, VLT/MUSE, and ALMA data along USMG II sightlines in the redshift range  $2 < z < 6$  to identify the disturbed cold gas coun-

terparts at high redshift. The JWST and ALMA data is from A Spectroscopic survey of biased halos In the Reionization Era (ASPIRE) JWST GO1 survey (P.I. F. Wang, Program ID: 2078) and Cycle 9 large program (P.I. F. Wang, Program ID:2022.1.01077.L) for the 25 ASPIRE quasar fields, with ALMA band-6 mosaics. The VLT/MUSE data is from the MUSE-DEEP survey (P.I. R. Ellis, Program ID: 0103.A-0140). We report the discovery of two USMGII structures and galaxies in their vicinity. For one ultra-wide ( $\Delta v > 1000 \text{ km s}^{-1}$ ) cold gas structure with two USMGII systems at  $z \sim 4.87$ , we detected Ly $\alpha$  emission within a 200 kpc scale. For a USMGII at  $z = 2.5652$ , we detected a galaxy with prominent He I, [S III], and Paschen lines, along with significant dust continuum at an impacted parameter of 38 kpc. The USMGII-traced cold gas resides in the inner CGM region of the host galaxy.

In Figure 1, we plot the spatial distribution of the two disturbed cold gas structures and their environment. In the left panel, we show that the two Ly $\alpha$  emitters detected by VLT/MUSE are located at  $\sim 200$  kpc from the ultra-wide USMGII pair ( $\Delta v > 1000 \text{ km s}^{-1}$ ) along the sightline of J1306+0356. We present the two absorbing systems and the spectra of the two detected LAEs (significance  $> 2\sigma$ ) in Figure 2. The complete ions in these two absorbing systems and the Voigt profile fitting are shown in Extended Data Figure 3. In addition to Mg II, we detect Fe II, Mg I, Si II, Al II, Al III, C IV, and tentative detections of Zn II absorption lines. We denote the system at  $z = 4.8634$  as system 1 and the system at  $z = 4.8821$  as system 2. For Mg II lines, the Mg II( $\lambda 2803$ ) line in system 1 is blended with the Mg II( $\lambda 2796$ ) line in system 2. From the ionization state modeling (see Methods) and a comparison with our observation, we find that system 1 has lower metallicity, less dust, and is slightly more ionized than system 2, suggesting an internal transfer of metals and dust within this ultra-large disturbed absorbing gas structure. From Figure 2, we observe that LAE1 exhibits an asymmetric double-peaked profile with an extension on the red side towards the absorbing system at  $z = 4.8821$ . We tentatively suggest that LAE1 is kinematically moving from the absorbing system at  $z = 4.8634$  towards the one at  $z = 4.8821$ , tracing the filaments of dense and cold (likely neutral) gas that connect these ultra-wide absorbing systems. We estimate the overdensity based on the two LAEs and find that the absorbing gas structure resides in an overdense region with  $\delta \sim 10^4$  (see Methods).

In the right panel of Figure 1, we show the de-

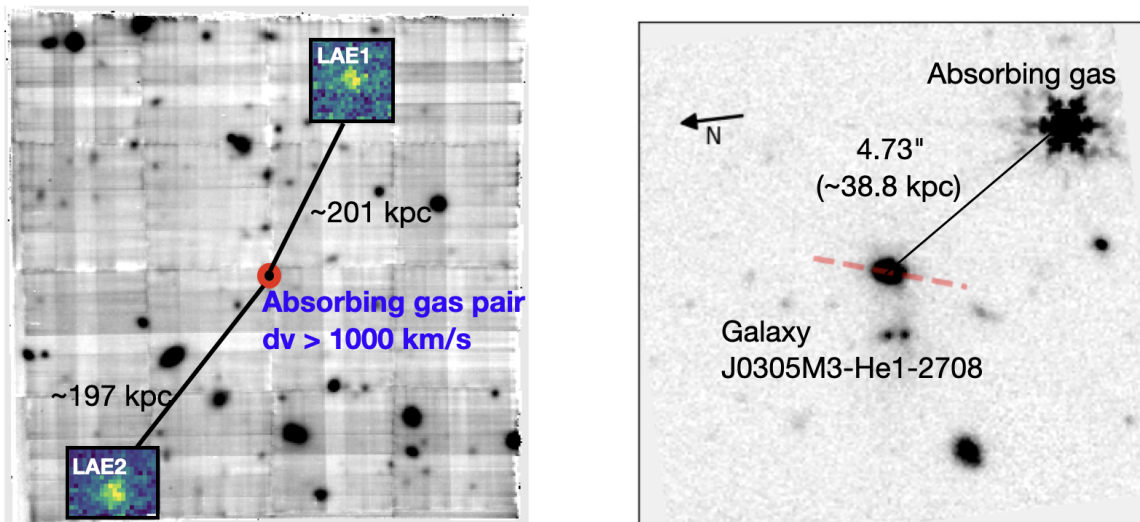


Figure 1: *Left.* Spatial distribution of the absorbing gas along J1306+0356 (located at the center of the VLT/MUSE cube) and the two LAEs, which are offset by  $\sim 200$  kpc from the gas. Narrow-band images of the two detected LAEs are presented. The absorbing gas structure is composed of two USMGII systems, with a total velocity width  $\Delta v$  greater than  $1000 \text{ km s}^{-1}$ . *Right.* Spatial distribution of the absorbing gas along the J0305–3150 sightline (upper right corner) and the host galaxy, as detected with JWST/NIRCam data. The red dashed line is the fitted galaxy major axis.

tection of a galaxy, J0305M31-He1-2708 (RA, Dec = 03:05:17.09,  $-31:50:49.20$ ), at an impact parameter of 38 kpc from the USMGII along J0305–3150 at  $z = 2.5652$ . Figure 3 presents the Magellan/FIRE spectrum of the strong Mg II absorption lines and the JWST/NIRCam 2D imaging of the galaxy, along with its nebular emission line 1D spectra. This galaxy exhibits prominent He I( $\lambda 10830$ ), [S III]( $\lambda 9531$ ), [S III]( $\lambda 9067$ ), and Pa $\gamma$  lines. The He I( $\lambda 10830$ ) line displays a double-peaked profile. Using ALMA data (see Extended Data Figure 1), we observe significant dust content in this galaxy, indicating a star formation rate (SFR) of  $(121 \pm 33) M_{\odot}/\text{yr}$  (see Methods). Table 1 presents the measurements of all the emission lines and the dust content of J0305M31-He1-2708. Given that a massive disk galaxy can host a DLA at  $z \sim 4$ <sup>34</sup>, we test the role of USMGII-traced cold gas in disk formation at  $z \sim 2.6$ .

From galaxy morphology fitting (see Methods and Figure 5), we find that our USMGII host is a disk-like galaxy. From the spectral energy distribution (SED) fitting (see Extended Data Figure 2), we obtain a best-fit stellar mass of  $\log(M/M_{\odot}) = 10.73^{+0.02}_{-0.60}$ . By comparing the effective radius  $R_e$  and stellar mass of the USMGII host galaxy with the massive galaxy size-mass relation

(halo mass greater than  $10^{10} M_{\odot}$ ) at  $z \sim 2.7$ <sup>35</sup>, we find that our galaxy lies between late-type and early-type galaxies, plausibly undergoing a transition phase between the two.

We further apply kinematic modeling to the grism spectra of the nebular emission lines and obtain a disk rotation velocity of  $v_{\text{rot}} = 115^{+97}_{-86} \text{ km s}^{-1}$  (see Methods and Figure 6), indicating a tentative rotating disk in galaxy J0305M31-He1-2708. Furthermore, we compare similar disk galaxies at  $z \sim 3$  (in terms of  $v_{\text{rot}}$ , stellar mass, and  $R_e$ ) and their H I content in cosmological simulations. We find that cold, high-column-density H I gas resides between the major and minor axis and exhibits angular momentum that is not perpendicular to the disk plane, suggesting its dynamical complexity. Given the outflow features observed in the JWST NIRCam imaging (F200W and F356W), the tentatively rotating disk, the galaxy type, and the kinematically extended ultra-strong absorbing cold gas, we propose that the cold gas traced by the USMGII drives disk and star formation in its host galaxy while simultaneously being influenced by galactic outflows.

In summary, we use ultra-strong and kinematically wide Mg II absorbing systems at  $z > 2$  to trace disturbed

cold and cool gas. We search for USMGII absorber galaxy counterparts using VLT/MUSE, JWST, HST, and ALMA data. We identify an ultra-strong and metal-enriched absorbing system (with two USMGIIIs) with a velocity width greater than  $1000 \text{ km s}^{-1}$ , accompanied by two surrounding LAEs at an impact parameter of approximately 200 kpc. The two absorbing systems exhibit interactions in metals, dust, and ionization, and are possibly connected by  $\text{Ly}\alpha$  emitting gas. Another USMGII system at  $z \sim 2.5$  resides in the CGM (with  $D = 38$  kpc) of a massive dusty star-forming galaxy, likely with a tentative rotating disk in its host galaxy. We find that the USMGII-traced cold gas resides in complex environments, both kinematically and dynamically. The cold gas is plausibly affects the disk formation and evolution, as well as large-scale structure at high redshift.

## Methods

**Cosmology** Throughout this work, we adopt the standard  $\Lambda$ CDM model with the following cosmological parameters:  $H_0 = 70 \text{ km s}^{-1} \text{ Mpc}^{-1}$ ,  $\Omega_\Lambda = 0.69$ , and  $\Omega_m = 0.31$ .

**Parent Absorber Sample** The parent sample of the Mg II absorber catalogs is from Chen et al., (2017)<sup>3</sup> and Zou et al., (2021)<sup>4</sup> (hereafter C17 and Z21). C17 comprises the Magellan/FIRE sample of 100 quasars with emission redshifts between  $z = 3.55$  and  $z = 7.09$ , with an average spectral resolution of  $R \sim 6000$ <sup>36</sup>. Z21 includes Gemini near-infrared spectroscopy of 51 quasars at  $z > 5.7$ , with an average spectral resolution of  $R \sim 800$ <sup>37</sup>. Considering the uncertainties in the equivalent width measurements, we pre-select the initial sample based on the criteria of  $W_r > 2.0 \text{ \AA}$  and  $\Delta v > 500 \text{ km s}^{-1}$ , rather than  $W_r > 3.0 \text{ \AA}$ , to avoid missing potential targets. After this step, we checked ancillary data from three sources: archival VLT/MUSE data, the JWST GO1 survey A Spectroscopic Survey of Biased Halos in the Reionization Era (ASPIRE), and ASPIRE-ALMA data. The final sample is presented in Table 1. We re-measure the equivalent width and velocity width of the absorption lines for the systems in QSO J1306+0356 and J0305–3150 using the Magellan/FIRE spectra and present the measurements in Table 1. For the other systems, the equivalent widths and  $\Delta v$  are taken from C17.

**VLT/MUSE data** The MUSE data used to search for  $\text{Ly}\alpha$  emitters in the quasar field of J1306+0356 is collected from the MUSE-DEEP survey (P.I. R. Ellis, Program ID: 0103.A-0140). We used the ESO MUSE data

reduction pipeline<sup>38,39</sup> to reduce the datacube. The ESO pipeline reduction process is briefly described as follows: First, we process the raw datacube using the ESO MUSE pipeline v2.8.9. Daily calibrations and the geometry table are used to generate pixel information, including location, wavelength, photon count, and variance estimates. Each exposure was precisely recentered to correct for derotator wobble. We then use the *scipost* recipe to perform astrometric and flux calibrations on the pixtable. The final datacube was generated using the *makecube* recipe. Sky background subtraction was performed using the ZAP process<sup>40</sup>. For the inter-stack masking, we run the *scibasic* and *scipost* recipes twice: the first time without using the specific bad pixel table, and the second time with it. Using the output of the ‘bad-pixel’ version of the cube, we derive a new, 3D mask which we apply to the original cube, effectively removing the inter-stack bad data.

**JWST/NIRCam data** The JWST data is taken from the A Spectroscopic survey of biased halos in the Reionization Era (ASPIRE) JWST GO1 survey (P.I. F. Wang, Program ID: 2078). The science goal of this program is driven by the study of supermassive black hole growth, its connection with the host galaxy, and metal enrichment during the reionization epoch. The full data JWST/NIRCam WFSS data reduction is described two ASPIRE early papers<sup>41,42</sup>. We perform data using version 1.10.2 of the JWST Calibration Pipeline (CALWEBB). For data calibration, we employ reference files (jwst 1080.pmap) from version 11.16.21 of the standard Calibration Reference Data System (CRDS). All imaging data in this study align with the Gaia data release 3. We adopt the method outlined in Sun et al., (2022)<sup>43</sup> which includes a column-average correction for 1/f-noise. This model traces point sources observed in the Large Magellanic Cloud field.

**ALMA data** The ALMA data used in this work is from the Cycle 9 large program (P.I. F. Wang, Program ID: 2022.1.01077.L) for the 25 ASPIRE quasar fields with ALMA band-6 mosaics. The data reduction was processed with the CASA pipeline v6.4.1.12. The full details of the ALMA data reduction are presented in Sun et al., (2024)<sup>44</sup>. For the continuum imaging, we flagged all spectral channels with a velocity offset smaller than  $500 \text{ km s}^{-1}$  from the quasar [C II] line center. Noisy spectral channels caused by telluric absorption were also visually identified through *plotms* and flagged from the continuum imaging. We then split the measurement sets to a channel width of 125 MHz and obtained continuum

<sup>1</sup><https://www.eso.org/sci/software/pipelines/muse/>

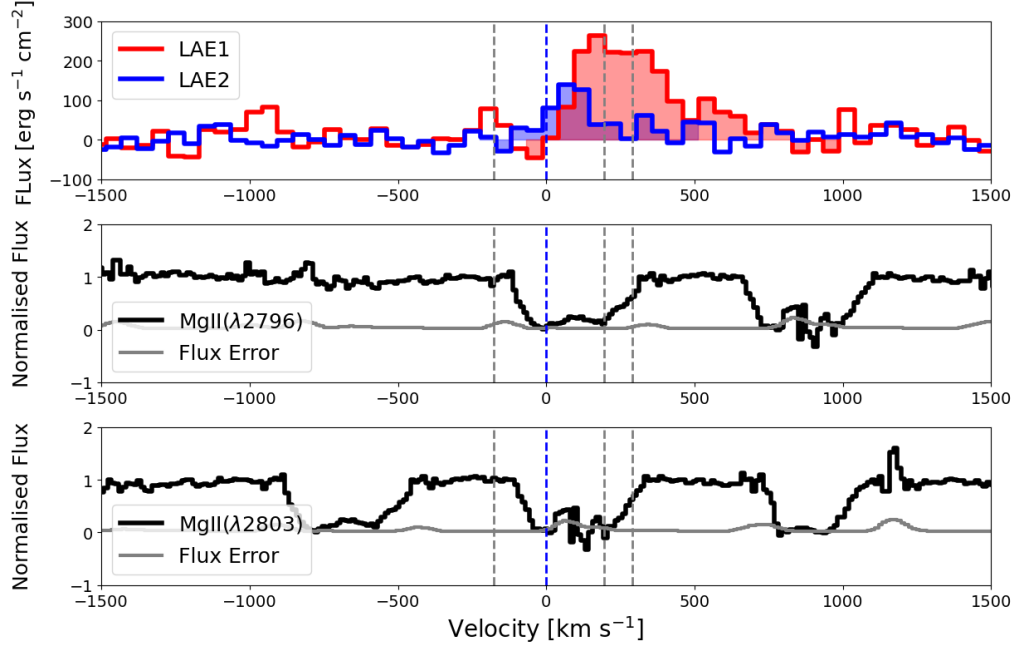


Figure 2: Emission profile of the  $\text{Ly}\alpha$  lines detected with VLT/MUSE and the absorption profile of the  $\text{Mg II}$  absorber observed by Magellan/FIRE along the J1306+0356 sightline at  $z = 4.8651$ , shown in velocity space. The  $\text{Ly}\alpha$  emitters are located at  $z = 4.867$ , at distances of 201 kpc (red) and 197 kpc (blue) from the absorbing gas, respectively. The gray and blue dashed lines in the  $\text{Mg II}$  profile indicate the positions of sub-components, with the blue dashed line marking  $\Delta v = 0 \text{ km s}^{-1}$ .

imaging at native resolution (robust=0.5, no uv-tapering; typical beam size is about  $0.7''$ ) and tapered resolution (robust=2.0, uv-tapered with a Gaussian kernel of full-width-half-maximum (FWHM) of  $1.0''$ ).

**Photometric data** For sightline J1306+0356, we use archival Hubble Space Telescope (HST) F770W and F850LP imaging data to estimate the LAE UV continuum. For sightline J0305–3150, we use multiband photometry from JWST (F115W, F200W, F356W) and HST (F105W, F125W, F160W, F606W, and F814W bands) for the SED fitting.

**Detection limits** We list six sightlines with USMGII absorbers and archival VLT/MUSE data covered in Table 1. Except for the deepest 10-hour exposure datacube in the field of J1306+0356, we do not detect  $\text{Ly}\alpha$  emission in the other five MUSE datacubes. The flux detection limits for the 10-hour MUSE-Deep single-point data and 1-hour MUSE-Wide data are  $3.1 \times 10^{-19} \text{ erg s}^{-1} \text{ cm}^{-2}$ <sup>38</sup> and  $2.0 \times 10^{-17} \text{ erg s}^{-1} \text{ cm}^{-2}$ <sup>45</sup>, respectively. For JWST/NIRCam WFSS data in the F356W band, the  $5\sigma$  line detection limit can reach  $2.0 \times 10^{-18} \text{ erg s}^{-1} \text{ cm}^{-2}$  by integrating the spectra over  $50 \text{ \AA}$ <sup>41</sup>, which corresponds to

a luminosity limit of  $1.1 \times 10^{40} \text{ erg s}^{-1}$  at  $z = 2.5$ .

**Emission line search** We search for  $\text{Ly}\alpha$  emission in the MUSE field using a simple SExtractor-based Python tool, MUSELET<sup>2</sup>. MUSELET uses SExtractor<sup>346</sup> to search for emission lines in narrowband (nb) imaging. The process is as follows: First, MUSELET creates a variance-weighted white light image and RGB images based on one-third of the wavelength range each. Next, MUSELET runs SExtractor on the nb files and generates a catalog that distinguishes sources with continuum emission. The continuum is extracted from a range of 20 wavelength pixels around the  $\text{Ly}\alpha$  emission line. We then visually inspect the catalog and rule out lines at lower redshifts. The final detected two LAEs are presented in Figure 2, both exhibiting a double-peaked  $\text{Ly}\alpha$  profile.

For the USMGII at  $z = 2.5652$  along the quasar sightline J0305–3150, we searched for the  $\text{S III}$ ,  $\text{He I}(\lambda 10830)$ , and Paschen $\gamma$  lines using JWST/NIRCam imaging and spectra, with a method similar to the one we used for the  $[\text{O III}]$  and  $\text{H}\beta$  line search at  $z = 5.7 - 6.5$ <sup>41</sup>. We iden-

<sup>2</sup><https://mpdaf.readthedocs.io/en/latest/muselet.html>

<sup>3</sup><http://www.astromatic.net/software/sextractor>

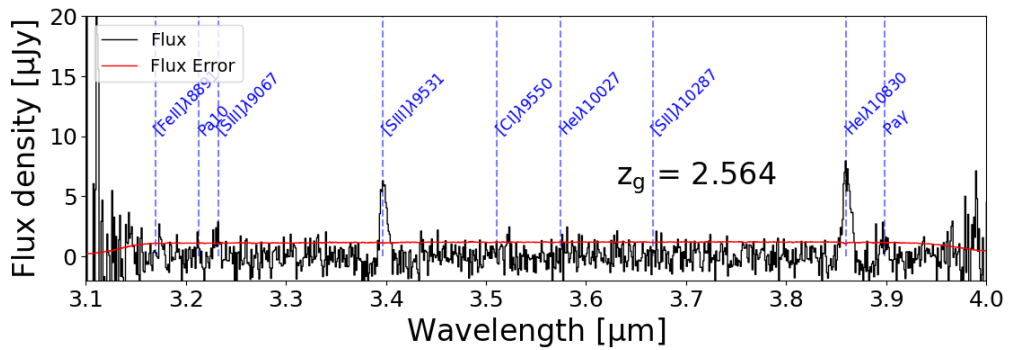
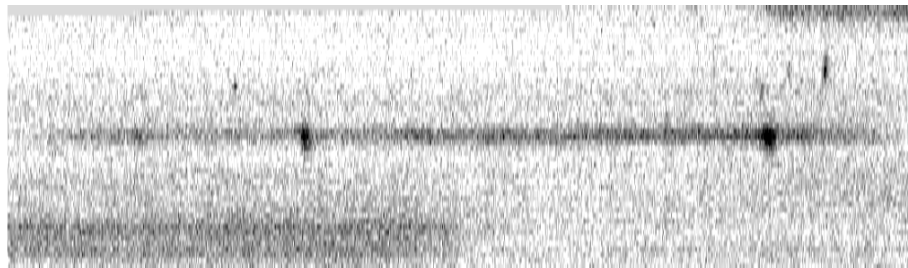
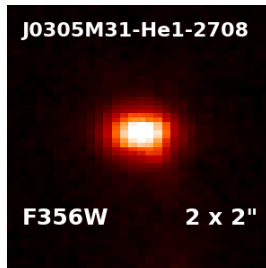
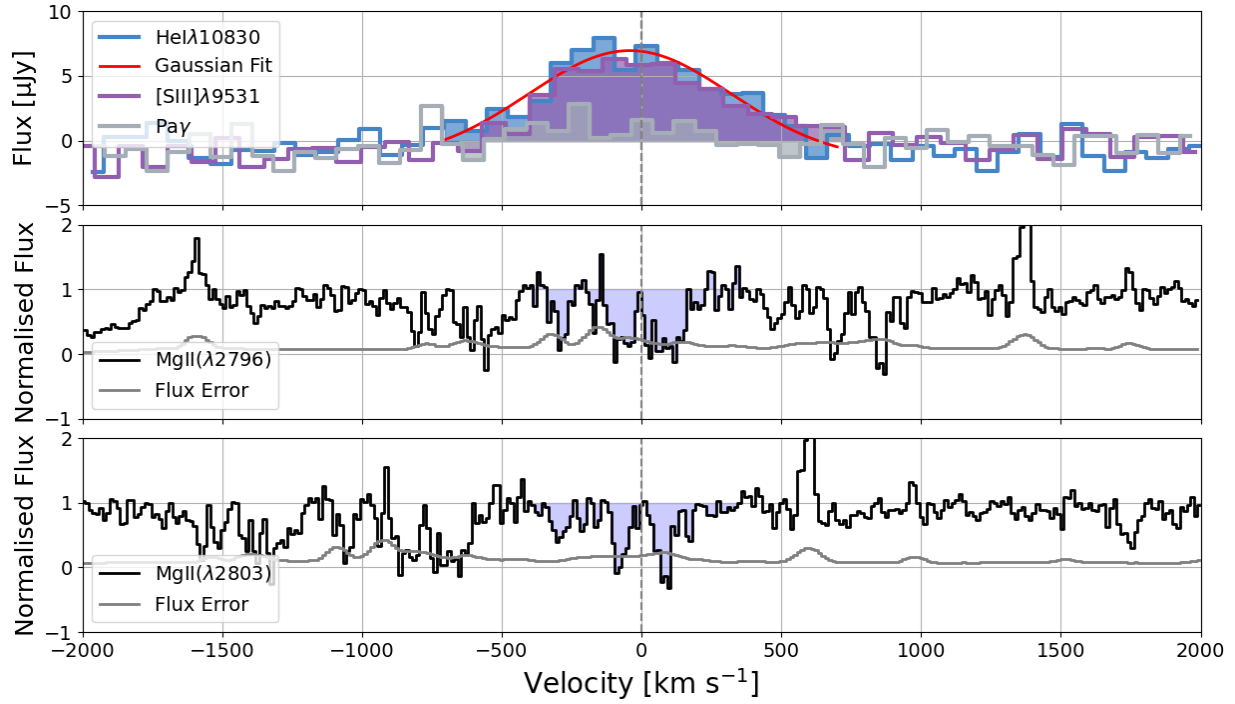


Figure 3: *Upper* : The absorption profiles of the USMGII at  $z = 2.5652$ , along with the 1D spectra of the detected galaxy which is 4.65'' (38 kpc) away from the absorber. The galaxy shows He I, [S III], and Paschen emission lines at  $z = 2.5643$  in the JWST NIRCcam F356W band. *Lower*: The 2D and 1D spectra of the host galaxy of the USMGII absorber. The cutout imaging size is  $2 \times 2''$ .

tified flux peaks with  $S/N > 3$  from the 1D spectra and applied a Gaussian filter template for the He I and [S III] lines to select potential candidates. The selected targets were then visually inspected by more than three people to determine the final set of emission-line galaxies.

**Absorption line measurements** The USMGII detected at  $z_{abs} = 4.8651$  towards quasar J1306+0356 ( $z_{em} = 6.02$ , R.A. = 13:06:08.27, DEC = +03:56:26.36) is reported with  $W_r = 2.804 \text{ \AA}$  and a velocity spread of  $\Delta v = 180.8 \text{ km s}^{-1}$  in C17. After our re-measurements of the EW and  $\Delta v$ , we report a new system at  $z = 4.8821$ , which is offset by around **1000**  $\text{km s}^{-1}$  from the system at  $z = 4.8651$ . The second system has an  $W_r(\text{Mg II}(\lambda 2803)) = 2.371 \pm 0.097 \text{ \AA}$  and  $\Delta v = 421.9 \text{ km s}^{-1}$ . We redefine the centers of these two systems at the positions of the strongest Mg II( $\lambda 2796$ ) subcomponents, with  $z = 4.8634$  and  $z = 4.8821$ , respectively.

In Table 2, we present the  $W_r$  of system 1 Mg II( $\lambda 2796$ ) line, system 2 Mg II( $\lambda 2803$ ) line, and the blended region. For C IV lines, there is also possible blending between C IV( $\lambda 1550$ ) in system 1 and C IV( $\lambda 1548$ ) in system 2. To simplify the analysis, we use the red and blue shaded regions in Extended Data Figure 3 to measure the  $W_r$  of C IV( $\lambda 1548$ ) and C IV( $\lambda 1550$ ) for the two absorption systems, respectively.

From Table 2, we observe that in general, system 2 has higher  $W_r$  for most ions, except for Al III, C IV, and slightly weaker Mg I lines. Given that system 1 has weaker intermediate ions but stronger high-ionization lines, it appears to be more ionized and less dusty than system 2. Mg II and C IV in the two systems are strongly blended with each other and probably saturated, it is impossible to obtain the accurate column density of these two ions. Fe II( $\lambda 2600$ ) is strongly affected by sky lines. Al III( $\lambda 1862$ ) and Zn II( $\lambda 2062$ ) are likely blended with other lines in system 2. We fit the other lines with a Voigt profile using the VPFIT program code<sup>47</sup>. The fitted profile is plotted in Extended Data Figure 3 and presented in Table 2. Given that saturation may still occur for optically thick lines, we are cautious about the absolute column density measurements for the ions. However, we focus on the relative metallicity between these systems in this work.

**Ly $\alpha$  emission around the USMGII at  $z = 4.867$  in the J1306+0356 field** Using MUSELET, we obtain the initial Ly $\alpha$  candidates in the J1306+0356 field. We then visually inspect the candidates by examining their 2D and

1D spectra, confirming two LAEs: LAE1 at RA, Dec = 196.5397, 3.9328; and LAE2 at RA, Dec = 196.5312, 3.9483. The spectra of the two LAEs and the USMGII absorber are presented in Figure 2. The  $v = 0 \text{ km s}^{-1}$  corresponds to  $z = 4.8634$ . The peak of LAE1’s main component and the blue bump are consistent with the centers of the USMGII subcomponents.

We then measure the equivalent width (EW) of the Ly $\alpha$  emission. The EW of the Ly $\alpha$  line is defined as the ratio of the Ly $\alpha$  line luminosity to the UV continuum luminosity density at Ly $\alpha = 1215.67 \text{ \AA}$ <sup>48</sup>:

$$EW = \int^{\lambda_1} \lambda_2 \frac{f_{\text{Ly}\alpha}^{\text{line}} - f_{\text{Ly}\alpha}^{\text{cont}}}{f_{\text{Ly}\alpha}^{\text{cont}}} d\lambda \quad (1)$$

where  $f_{\text{Ly}\alpha}^{\text{line}}$  and  $f_{\text{Ly}\alpha}^{\text{cont}}$  are the flux densities of the Ly $\alpha$  line and the continuum, respectively. We measure the Ly $\alpha$  line flux from the extracted 1D spectra, including the blue bump. We find the fluxes of LAE1 and LAE2 to be  $f(\text{LAE1}) = 2.45 \pm 0.80 \times 10^{-17} \text{ erg s}^{-1} \text{ cm}^{-2}$  and  $f(\text{LAE2}) = 0.67 \pm 0.31 \times 10^{-17} \text{ erg s}^{-1} \text{ cm}^{-2}$ , respectively. We then use archival Hubble Space Telescope (HST) F770W and F850LP data to estimate the UV continuum magnitude and flux density upper limit. From this, we calculate the EWs of LAE1 and LAE2 to be **73.15  $\pm$  24.05  $\text{\AA}$**  and **20.01  $\pm$  9.27  $\text{\AA}$** , respectively. The luminosities of LAE1 and LAE2 are  $L_{\text{Ly}\alpha} = (6.32 \pm 2.08)$  and  $(2.45 \pm 0.81) \times 10^{42} \text{ erg s}^{-1}$ , respectively. The FWHM of LAE1 is  $121 \pm 22 \text{ km s}^{-1}$ , corrected for instrumental broadening using the MUSE line spread function. We estimate the star formation rate (SFR) of LAE1 from the Ly $\alpha$  luminosity, using the SFR-H $\alpha$  relation<sup>49</sup> and the Ly $\alpha$ -H $\alpha$  emissivity ratio<sup>50</sup>:  $\text{SFR}(\text{Ly}\alpha) = 9.1 \times 10^{-43} \times L(\text{Ly}\alpha) M_{\odot}/\text{yr}$ , yielding  $\text{SFR}(\text{Ly}\alpha) = 5.75 \pm 1.89 M_{\odot}/\text{yr}$ . This SFR value is consistent with the previous statistical results of LAE SFR<sup>51</sup>, which measure  $\text{SFR}(\text{Ly}\alpha)$  at  $z > 2.1$ . Details of these two LAE measurement are presented in Table 1.

**Comparison with other LAEs and DLA hosts** In order to place our detected LAE in the context of other star-forming galaxies at similar redshifts, we compare our USMGII LAEs’ Ly $\alpha$  emission line flux, luminosity, and EW with those from other LAE surveys, DLA systems, and Mg II hosts. In the upper panel in Figure 4, we plot the Ly $\alpha$  line flux in the DLA host against the DLA log  $N(\text{H I})$ , with the colormap of velocity width ( $\Delta v$ ) of Si II. The full DLA-host sample is collected in Krogager et al., (2017)<sup>52</sup>. We extrapolate the  $N(\text{H I})$  of our Mg II system

1 from the EW of Mg II( $\lambda 2796$ ) using the relation in Lan et al. (2018)<sup>7</sup>:

$$N_{\text{H I}} = A \left( \frac{W_{\lambda 2796}}{1 \text{ \AA}} \right) (1+z)^\beta \quad (2)$$

where  $A = 10^{18.96 \pm 0.10} \text{ cm}^{-2}$ ,  $\alpha = 1.69 \pm 0.13$ , and  $\beta = 1.88 \pm 0.29$ . We obtain  $\log N(\text{H I})$  is  $21.19 \pm 0.03$  for system 1. Except for one exceptionally bright Ly $\alpha$  emission from a DLA host in Krogager et al., (2015)<sup>53</sup>, we find that the stronger  $N(\text{H I})$  is, the brighter the host's Ly $\alpha$  emission. Our detected Mg II surrounding LAE is consistent with this trend. We also note that the strength of Ly $\alpha$  emission does not show a significant correlation with the velocity width of the absorption line. In the lower panel of Figure 4, we plot the Ly $\alpha$  EW from the survey in MUSE Hubble Ultra Deep<sup>54,55</sup> and the JWST Advanced Deep Extragalactic Survey (JADES) survey<sup>56</sup>. We find that the EW of our USMGII-LAE1 ( $> 3\sigma$ ) is consistent with the median EW of LAE measured at  $z \sim 4.9$ <sup>54</sup>.

**Possibility of overdensity** We estimate the random field number density ( $N_{\text{gal}}/\text{cMpc}^3$ ) of LAEs at  $z \sim 4.8$  using the Ly $\alpha$  luminosity function measured from the MUSE Hubble Deep data<sup>57</sup>. For  $\log L_{\text{Ly}\alpha} > 42.0$ , the  $\Phi(\log L > 42/\text{cMpc}^3)$  is about  $10^{-2}$ . Given that our two LAEs ( $> 2\sigma$ ) have a redshift difference of  $\Delta z = 0.002$ , the number density within the comoving volume (MUSE FoV times  $\Delta z$ ) is  $1.14 \times 10^{-4} \text{ Mpc}^3$ . This suggests that the two LAEs and the USMGII gas reside in an overdense region with  $\delta \sim 10^4$ .

High  $N(\text{H I})$  gas in overdense regions has been detected at similar redshifts, and suggested that the cold gas content needs to be increased in fiducial cosmological simulations. Heintz et al., (2024a)<sup>58</sup> reported ten galaxies with strong DLA features at  $z = 5.4\text{--}6.0$  from JWST NIRSpec FRESCO (GO-18905, PI: Oesch) survey. The ten DLA-bearing galaxies reside in a foreground protocluster with more than 25 galaxies at similar redshifts ( $z = 5.35\text{--}5.40$ ). Such high  $N(\text{H I})$  and nearly neutral gas content in overdense regions at the end of the reionization epoch may play a key role in cosmic assembly history and the transition phase of IGM large-scale structure. Our detection of the metal-enriched and kinematically ultra-large system may further reveal baryonic transfer processes in these overdense regions at  $z \sim 5$ .

**Metallicity and ionization state of the ultra extended system** From Extended Data Figure 3, we see that the two absorbing systems share similar metal species, with

the bluer system ( $z = 4.8821$ ) exhibiting slightly higher equivalent widths in the Fe II, Si II, and Al II lines. Given that the two systems likely share a common origin and display an extremely large combined velocity width (greater than  $1000 \text{ km s}^{-1}$ ), we use CLOUDY<sup>59</sup> to model the ionization state, metallicity, and gas density of these systems.

Although we do not have direct measurements of  $N(\text{H I})$ , we can still derive the **relative** distribution of metallicity, dust content, gas density, and ionization state between these two absorbing systems. First, we varied the stopping column density of H I and found that when  $\log N(\text{H I}) < 18.0$ , even increasing the gas metallicity to solar could not reach the detected column densities of Si II, Al II, and Fe II. We then set  $\log N(\text{H I})$  between 20 and 22 (i.e., DLA systems) and varied the metallicity  $\log(Z/Z_\odot)$  between  $-3$  and  $1$ . The dust content was first scaled with metals and adjusted accordingly with changes in metallicity.

In all modeling results with varying metallicity, system 1 exhibits a metallicity that is  $\sim 1$  dex lower than that of system 2 (based on  $N(\text{Zn II})$ ). The ionization state parameter  $\log U$  of system 1 is about 0.7 dex lower than that of system 2, as indicated by the ratio of Al II to Al III. The ionization parameter  $U$  is defined as  $U = \Phi(\text{H})/(\text{n(H)} \times c)$ , where  $\Phi(\text{H})$  is the flux of ionizing photons and  $c$  is the light speed. Specifically, when  $\log N(\text{H I}) = 21.0$ , the  $\log(Z/Z_\odot)$  of system 1 and system 2 is  $-2.5$  and  $-1.5$ , respectively (see Extended Data Figure 4). Such metallicity range is also consistent with predictions of DLA at  $z \sim 4.8$  from the statistical metallicity distributions of large DLA samples<sup>60</sup>. We note that Si II exhibits overabundances compared to other elements, regardless of changes in metallicity and dust content. We also found that, for system 2, the modeled  $\log N(\text{Fe II})$  is consistently lower than the observed value by  $\sim 0.4$  dex, whereas for system 1, the modeled value is higher than the observed value by about 0.4 dex. Given that iron is more sensitive to dust depletion compared to silicon and zinc<sup>61</sup>, system 2 should contain more dust than system 1.

In summary, this kinematically ultra-wide ( $\Delta v > 1000 \text{ km s}^{-1}$ ) absorbing structure consists of two systems. The bluer system has lower metallicity, less dust, and is slightly more ionized than the redder one. Both systems share similar metal species and are likely connected by the Ly $\alpha$  emitting gas, residing in an overdense region at  $z \sim 5$ . We also keep the possibility that

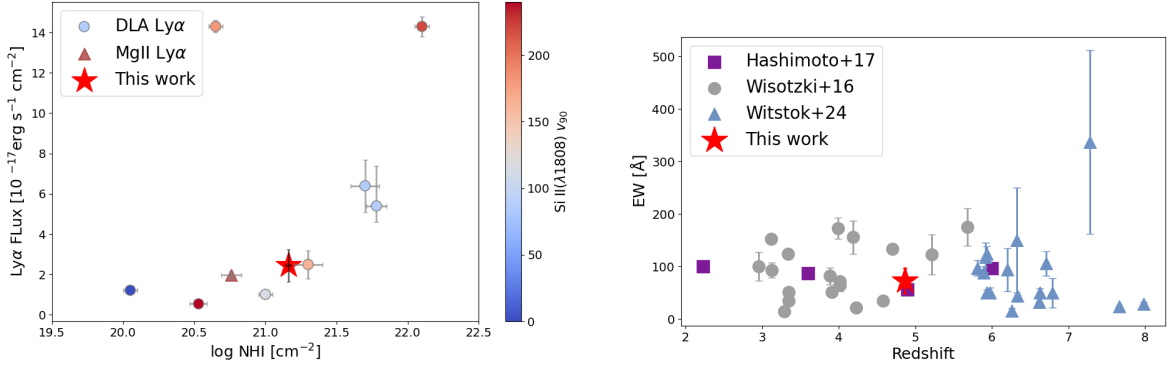


Figure 4: *Upper*: Comparison of USMGII-Ly $\alpha$  line flux with other DLA-Ly $\alpha$  hosts. The DLA-Ly $\alpha$  data points are color-coded by the velocity width  $v_{90}$  of the Si II( $\lambda$ 1808) line. The Mg II system ( $W_r = 2.033 \pm 0.187$  Å and  $v_{90}(\lambda 2796) = 355$  km s $^{-1}$ ) at  $z = 3.188$  in the MAGG survey<sup>29</sup> is plotted as a red triangle. The column density of H I for the two Mg II systems, including our  $z = 4.8651$  USMGII system, is extrapolated from the  $W_r(\text{Mg II})-N(\text{H I})$  relation<sup>7</sup>. *Lower*: Equivalent widths of LAEs detected in the MUSE Hubble Ultra Deep Field and the JADES survey at  $2 < z < 8$ .

fainter host galaxies or obscured massive galaxy(ies) are located closer to the absorbing gas structure. Based on the ASPIRE-ALMA results<sup>44</sup>,  $66 \pm 7\%$  of star formation at  $z \sim 5$  remains obscured.

**Nebular emission lines around the USMGII absorber at  $z = 2.5652$  in the J0305-3150 field** We detect a galaxy counterpart ASPIRE J0305M31-HeI-2708 in the J0305–3150 field with prominent He I( $\lambda$ 10830), [S III]( $\lambda$ 9531), [S III]( $\lambda$ 9067), Pa $\gamma$  and Pa10 lines. Profiles of the absorbing gas and galaxy are presented in Figure 3. From Equation 1 and the Mg II ( $\lambda$ 2796) equivalent width, we estimate the absorbing gas to have a H I column density of  $\log N(\text{H I}) = 20.77 \pm 0.12$ . Full details of the emissions are presented in Table 1. The FWHM of He I line is around 710 km s $^{-1}$ , with instrument broadening corrected using NIRCcam Grism LSF function<sup>62</sup>. The flux ratio between He I and Pa $\gamma$  line is 2.7.

We measure the EW of the emission lines with the F115W, F200W and F356W photometric data and the line flux. The target continuum flux densities is modelled with a power-law  $f_{cont} = \lambda^\alpha$ . Then we estimate the flux densities at the emission lines and measure the EW following same method in Equation 1.

**Stellar mass, Dust Continuum and SFR** We also detected dust continuum in the galaxy J0305M50-HeI-2708 using ASPIRE-ALMA data (noted as J0305M50.C04, see Figure 1). The details of searching dust continuum and [C II] emitters at  $z > 4$  using the ASPIRE-ALMA

data is presented in Sun et al., (2024)<sup>44</sup>.

The aperture and peak fluxes of the J0305M3150.C04 source are  $0.42 \pm 0.11$  mJy and  $0.40 \pm 0.03$  mJy, respectively. We calculate the far-infrared SFR following the relation from<sup>63</sup>:  $\text{SFR} = 2.1 \times 10^{-10} L_{\text{FIR}(\text{SF})} [M_\odot \text{ yr}^{-1}]$ , where  $L_{\text{FIR}}$  is the far-infrared luminosity. The  $L_{\text{FIR}}$  is determined by SED fitting of a black body in the 42.5–122.5  $\mu\text{m}$  range. We adopt an average dust temperature of 35 K and a dust emissivity index  $\beta$  of 1.6<sup>64</sup>. We then calculate the dust mass and  $L_{\text{FIR}(\text{SF})}$ , which are found to be  $(1.98 \pm 0.55) \times 10^8 M_\odot$  and  $(5.74 \pm 1.58) \times 10^{11}$  erg s $^{-1}$ , respectively. The resulting SFR is  $120 \pm 33 M_\odot \text{ yr}^{-1}$ , indicating intense star formation in this galaxy.

We compare our detected dusty SFG with DLA hosts detected by ALMA at  $z = 2-4$ <sup>30,64,65</sup>. The SFR of our USMGII counterpart is consistent with the SFR of DLA submillimeter-detected hosts ( $\sim 110 M_\odot \text{ yr}^{-1}$ ).<sup>30</sup> report a moderate SFR ( $\sim 20 M_\odot \text{ yr}^{-1}$ ) for the DLA host J1201+2117, which is claimed to be undergoing a major merger at  $z \sim 3.79$ .

The stellar mass of the galaxy is obtained using the spectral energy distribution fitting tool BAGPIPES<sup>66</sup>. We use multiband photometry from JWST (F115W, F200W, F356W) and HST (F105W, F125W, F160W, F606W, and F814W bands) as inputs. We adopt a constant star formation history (SFH) and the Calzetti dust law<sup>67</sup>, allowing  $A_V$  to vary between 1.0 and 5.0, metallicity ( $\log Z/Z_\odot$ ) to vary between  $-2$  and  $2$ , and age to

vary between 100 Myr and 2.5 Gyr. The best-fitted stellar mass of the galaxy is  $\log(M/M_\odot) = 10.73^{+0.02}_{-0.60}$  (see Figure 2). The difference in the stellar mass varies by around 0.2 when adopting a post-starburst SFH.

**Galaxy morphology** We use the galaxy decomposition tool GALFIT<sup>68,694</sup> to fit the position angle (PA) and Sérsic index of this SFG. We note that J0305M31-He1-2708 exhibits different morphologies in the F200W and F356W bands, so we fit the F200W and F356W bands individually. The fitted PA angles are plotted in Figure 5. The Sérsic indices in F200W and F356W are  $1.16 \pm 0.02$  and  $1.46 \pm 0.02$ , respectively, indicating a tentative disk-like structure based on the disk galaxy classification criteria<sup>70</sup>. The effective radius ( $R_e$ ) and  $b/a$  of the galaxy in F200W are  $1.59 \pm 0.01$  kpc and  $0.54 \pm 0.01$ , respectively, and in F356W they are  $0.93 \pm 0.01$  kpc and  $0.54 \pm 0.01$ . We compare our measured galaxy  $R_e$  in F200W and stellar mass with the empirical galaxy size (observed in the rest-frame 5000 Å)-mass relation at  $z \sim 2.7$ <sup>35</sup>, and find that our detected dusty SFG lies between early-type and late-type galaxies.

**Kinematics modeling** A DLA host harboring a rotational disk has been reported at  $z \sim 3-5$ <sup>34</sup>. Because USMGI systems have a high probability to be associated with a high H I column density, we discuss whether our host has a similar rotational disk at the cosmic noon. We first measure the velocity gradient of the He I  $\lambda 10830$  line following the method in Nelson et al., (2023)<sup>72</sup>. For each row of the grism 2D spectra along the dispersion direction, we fit a light-weighted center using a Gaussian profile. We then calculate the differences between the light-weighted center of the He I  $\lambda 10830$  line and the light-weighted center of the grism image. Note that the velocity derived from these two centers reflects contributions from both the spatial and kinematic properties of the line. Since we do not have multiple medium-band images to differentiate these two contributions, we can only constrain the  $v_{\text{rot}}$  limit.

The observed velocity of He I line is then calculated as  $v_{\text{obs}} = (v_{\text{max}} - v_{\text{min}})/2$  from the velocity map. For He I line, we find  $v_{\text{obs}} = 248 \pm 52$  km s<sup>-1</sup>. The rotation velocity,  $v_{\text{rot}}$ , is derived from  $v_{\text{rot}} = v_{\text{obs}} / \sin i$ , where  $i$  is the inclination angle. As mentioned in Nelson et al., (2023)<sup>72</sup>, the intrinsic  $q_0$  of the galaxy cannot be determined, so we assume  $0.05 < q_0 < q$  to estimate the uncertainties in  $v_{\text{rot}}$ , where  $q$  is the observed major-to-minor axis ratio. We note that the velocity dispersion is contributed

by both the instrument and the target. NIRCам has a resolution of  $R \sim 1550$  at  $\lambda \sim 3.5\mu\text{m}$ , corresponding to  $\sim 84$  km s<sup>-1</sup>. Considering the instrumental effect, the corrected  $v_{\text{rot}}$  for the galaxy and the emission line should be below 233 km s<sup>-1</sup>.

We then apply a dynamical modeling approach to the He I and [S III] lines to further assess the  $v_{\text{rot}}$ , following the method described in Li et al., (2023)<sup>71</sup>. The velocity map is obtained using a similar method as described above, followed by Markov chain Monte Carlo (MCMC) sampling to derive the best-fit kinematic parameters and their uncertainties. This method builds on the approach developed in Outini et al., (2020)<sup>73</sup>. For the He I line, we derive  $v_{\text{rot}} = 115^{+97}_{-86}$  km s<sup>-1</sup>, indicating a tentative rotating disk (see Figure 6).

**Comparison with in cosmological simulation** To further understand the kinematics and dynamics of metal-enriched cold gas and its role in disk and galaxy formation, we compare the H I gas distribution around similar disk-like galaxies (in terms of SFR,  $v_{\text{rot}}$ ,  $M_*$ , and  $R_e$ ) in the cosmological simulation IllustrisTNG100 (hereafter TNG-100)<sup>75</sup>. Disk-like galaxies are identified by requiring a disk mass fraction,  $f_{\text{disk}}$ , greater than 0.5. The  $f_{\text{disk}}$  values are obtained using the morphological decomposition method from Liang et al., (2024)<sup>74</sup>. We select 18 disk-like galaxies and find that high  $N(\text{H I})$  gas within 50 kpc of the host galaxies shows a high incidence between the major and minor axis. The angular momentum of the high  $N(\text{H I})$  gas is not perpendicular with the disk angular momentum, indicating dynamical complexity beyond simple inflow or outflow models. We present one example in Figure 7. We plot the column density distribution of H I gas and the angular momentum directions of the disk and H I gas. The H I gas is derived from the total hydrogen content in TNG100 using a post-processing model based on Gnedin & Kravtsov (2011)<sup>76</sup>.

From the simulation, we see that high density H I gas penetrates the hot CGM and then accretes onto the galaxy. Analytical models predict that the mode of cold gas accretion onto galaxies evolves with redshift. The fraction of cold-in-hot mode increases with redshift in a large-mass halo ( $M_h > 10^{12} M_\odot$ ) at  $z > 1$ <sup>77,78</sup>. The penetrated cold flow further sustains star and disk formation. Meanwhile, the turbulence and pressure instability in the inner CGM caused by cold flows enhance the probability of galactic outflows escaping from the galaxy. Therefore, the cold flow in high-mass halos plays a critical role in the complete virialization of the CGM, and consequently,

<sup>4</sup><https://users.obs.carnegiescience.edu/peng/work/galfit/galfit.html>

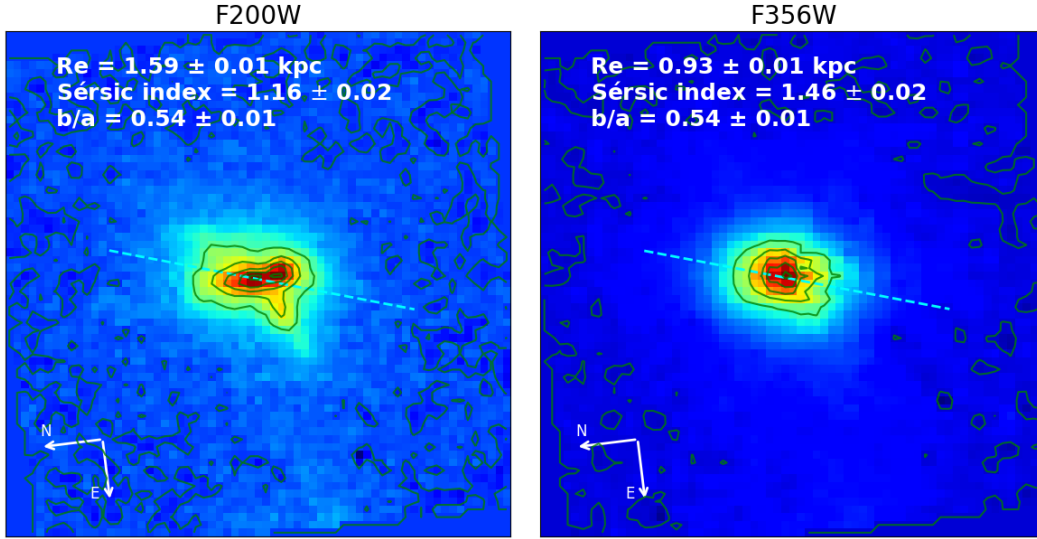


Figure 5: Contour map of galaxy J0305M31-He1-2708 in F200W (left) and F356W (right), respectively. We use GALFIT to fit the effective radius ( $R_e$ ), Sérsic index, major-to-minor axis ratio, and position angle of the galaxy. The cyan dashed line indicates the major axis of the galaxy.

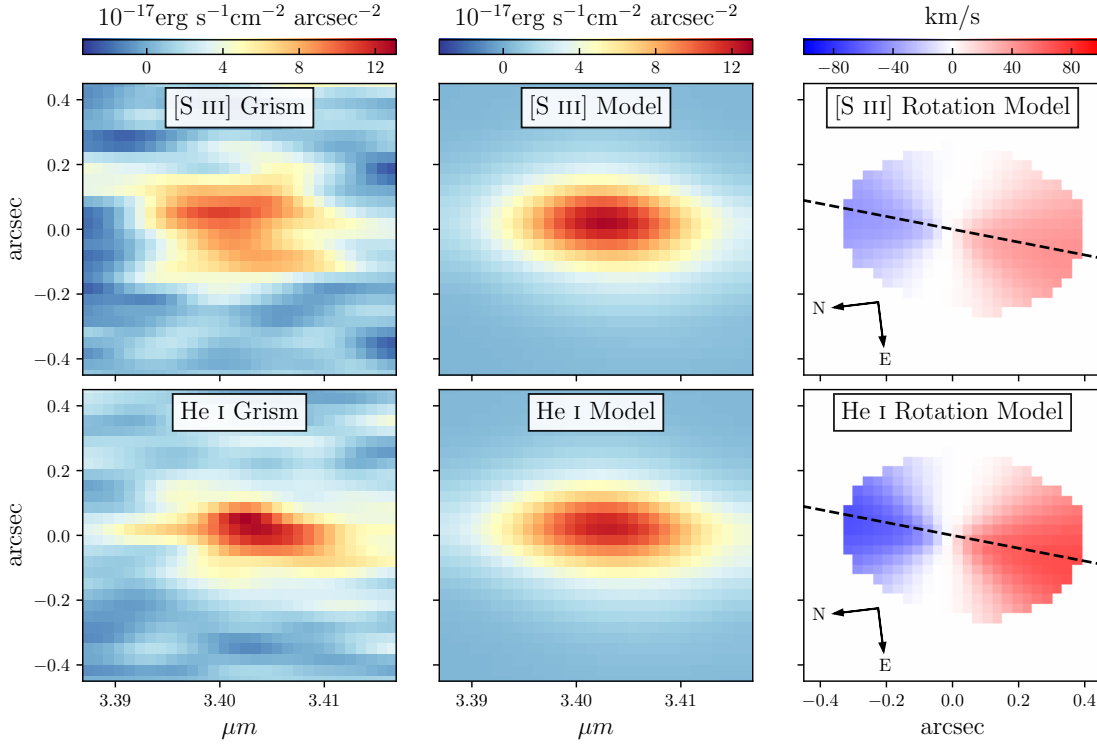


Figure 6: Kinematics modeling for He I and [S III] lines in J0305M31-He1-2708. The upper and lower panels are the [S III] and He I lines, respectively. From left to right, the panels show the real grism data, the best-fit Sérsic model convolved with the PSF, and the rotation modeling following the method in Li et al., (2023)<sup>71</sup>.

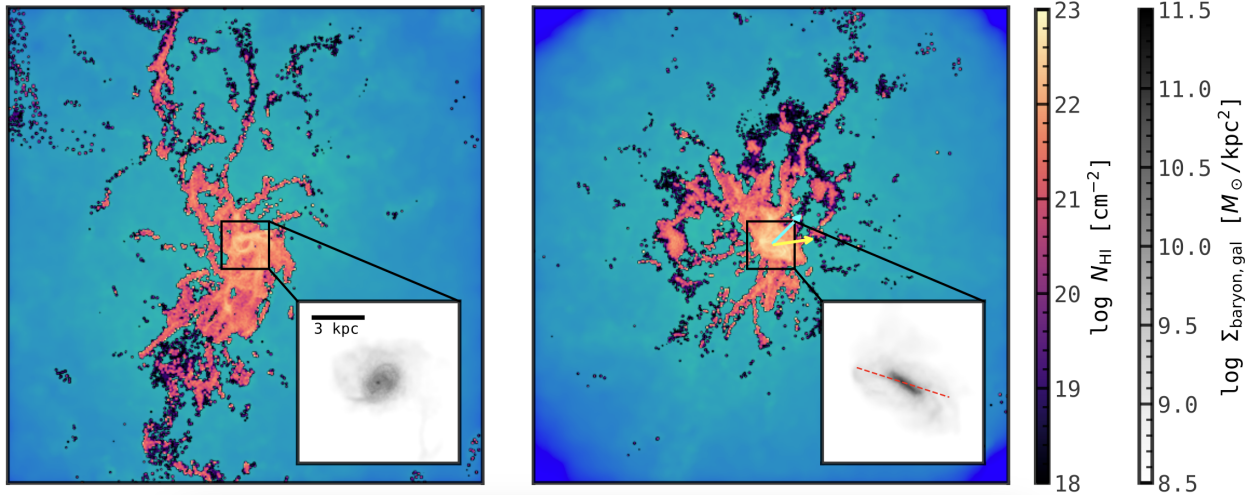


Figure 7: Example of the H I gas column density distribution around one disk galaxy at  $z \sim 3$  from TNG100, selected based on the disk-like galaxy criteria in Liang et al., (2024)<sup>74</sup>. The simulated galaxy has similar stellar mass, halo mass, SFR, and  $R_e$  to our detected galaxy. The left and right panels show face-on and edge-on views of the same galaxy on a  $100 \times 100$  kpc scale, respectively. The zoom-in box shows the stellar+gas content of the disk on a  $5 \times 5$  kpc scale. The red dashed line is the major axis of the galaxy. The blue and yellow arrows in the right panel indicate the angular momentum directions of the disk and H I gas, respectively.

in the transition of galaxies from star-forming to quiescent.

We estimate the halo mass of our detected SFG using the stellar-halo mass relation<sup>79</sup> and obtain  $\log(M_h/M_\odot) = 12.27^{+0.02}_{-0.60}$ . The virial radius is then calculated using the relation  $R_{\text{vir}} = (M_h / ((3/4)\pi \times 200 \times \rho_{\text{crit}}))^{1/3}$ , which gives  $R_{\text{vir}} = 245$  kpc. Our detected USMGII gas resides in the  $0.16 R_{\text{vir}}$ . Combining the host galaxy’s outflow-like features from JWST F200W and F356W imaging, its classification as not yet early-type, and the tentative rotating disk structure, we suggest that the high velocity USMGII gas is accreting onto the galaxy, supporting starburst and disk formation, while also being affected by the galactic outflow.

**Acknowledgements** We thank fruitful discussions with Weichen Wang, Valentina D’Odorico, Fengwu Sun, Pasquier Norderdaeme and Marta Galbiati. SZ acknowledges support from the National Science Foundation of China (no. 12303011). JBC acknowledges funding from the JWST Arizona/Steward Postdoc in Early galaxies and Reionization (JASPER) Scholar contract at the University of Arizona. WS and LCH acknowledge support from the National Key R&D Program of China (2022YFF0503401), the National Science Foundation of China (11991052, 12233001), and the China Manned Space Project (CMS-CSST-2021-A04, CMS-CSST-2021-A06). This

work is based on observations made with the Magellan/FIRE, NASA/ESA/CSA James Webb Space Telescope and Hubble Space Telescope, VLT/MUSE, and ALMA telescopes. The JWST data were obtained from the Mikulski Archive for Space Telescopes at the Space Telescope Science Institute, which is operated by the Association of Universities for Research in Astronomy, Inc., under NASA contract NAS 5-03127 for JWST. These observations are associated with program #2078. Support for program #2078 was provided by NASA through a grant from the Space Telescope Science Institute, which is operated by the Association of Universities for Research in Astronomy, Inc., under NASA contract NAS 5-03127.

**Author Information** The authors declare no competing interests.

**Author Contributions** SZ designed the project, led the data analysis, and drafted the main text. RAS, PPJ, and CP contributed to the text and major scientific discussions on the CGM-galaxy connection. JBC led the photometry catalog efforts for the ASPIRE team. FW, JY, and XF designed the JWST ASPIRE proposal and led the data reduction. JL, FZ, and LW contributed to the cosmological simulations and theoretical discussions. ZL contributed to the disk dynamical modelling. WS, LCH, and CC contributed to the GALFIT fitting process and disk galaxy discussion. J.Li contributed to the ALMA data analysis. JW and WL provided input on the outflow discussion. XL, SZ, CP, and EPF contributed to the VLT/MUSE data reduction. RAS led the Magellan/FIRE data reduction. All au-

thors contributed to the data interpretation and manuscript.

**Data availability** The VLT/MUSE raw data can be downloaded via the ESO archival data system. The JWST data presented in this paper were obtained from the Mikulski Archive for Space Telescopes (MAST) at the Space Telescope Science Institute. The specific observations analyzed can be accessed via DOI: 10.17909/vt74-kd84. Other reduced data underlying this article will be made available upon request to the corresponding author.

## References

1. Faucher-Giguère, C.-A. & Oh, S. P. Key Physical Processes in the Circumgalactic Medium. *Annu. Rev. Astron. Astrophys.* **61**, 131–195 (2023). 2301.10253.
2. Barnes, L. A., Garel, T. & Kacprzak, G. G. Ly- $\alpha$  and Mg II as Probes of Galaxies and Their Environment. *Publ. Astron. Soc. Pac.* **126**, 969 (2014). 1409.6320.
3. Chen, S.-F. S. *et al.* Mg II Absorption at  $2 < z < 7$  with Magellan/Fire. III. Full Statistics of Absorption toward 100 High-redshift QSOs. *Astrophys. J.* **850**, 188 (2017). 1612.02829.
4. Zou, S. *et al.* Strong Mg II and Fe II Absorbers at  $2.2 < z < 6.0$ . *Astrophys. J.* **906**, 32 (2021). 2010.11432.
5. Sebastian, A. M. *et al.* E-XQR-30: The evolution of Mg II, C II, and O I across  $2 < z < 6$ . *Mon. Not. R. Astron. Soc.* **530**, 1829–1848 (2024). 2403.10072.
6. Ménard, B. *et al.* Probing star formation across cosmic time with absorption-line systems. *Mon. Not. R. Astron. Soc.* **417**, 801–811 (2011). 0912.3263.
7. Lan, T.-W. & Mo, H. The Circumgalactic Medium of eBOSS Emission Line Galaxies: Signatures of Galactic Outflows in Gas Distribution and Kinematics. *Astrophys. J.* **866**, 36 (2018). 1806.05786.
8. Noterdaeme, P. *et al.* Discovery of a compact gas-rich damped Lyman- $\alpha$  galaxy at  $z = 2.2$ : evidence of a starburst-driven outflow. *Astron. Astrophys.* **540**, A63 (2012). 1202.0280.
9. Zou, S. *et al.* DESI Survey Validation Data in the COSMOS/Hyper Suprime-Cam Field: Cool Gas Trace Main-sequence Star-forming Galaxies at the Cosmic Noon. *Astrophys. J.* **960**, 34 (2024). 2302.13357.
10. Dutta, R. *et al.* MUSE Analysis of Gas around Galaxies (MAGG) - II: metal-enriched halo gas around  $z \sim 1$  galaxies. *Mon. Not. R. Astron. Soc.* **499**, 5022–5046 (2020). 2009.14219.
11. Wu, Y. *et al.* A Spectroscopic Survey of Biased Halos in the Reionization Era (ASPIRE): JWST Discovers an Overdensity around a Metal Absorption-selected Galaxy at  $z \sim 5.5$ . *Astrophys. J. Lett.* **956**, L40 (2023). 2309.16757.
12. Zou, S. *et al.* A Spectroscopic survey of biased halos in the Reionization Era (ASPIRE): Impact of Galaxies on the Circumgalactic Medium Metal Enrichment at  $z > 6$  Using the JWST and VLT. *Astrophys. J. Lett.* **963**, L28 (2024). 2402.00113.
13. Zou, S. *et al.* Near-infrared spectroscopic observations of high redshift C I absorbers. *Astron. Astrophys.* **616**, A158 (2018). 1710.05369.
14. Nestor, D. B. *et al.* Large-scale outflows from  $z \sim 0.7$  starburst galaxies identified via ultrastrong Mg II quasar absorption lines. *Mon. Not. R. Astron. Soc.* **412**, 1559–1572 (2011). 1003.0693.
15. Kacprzak, G. G. *et al.* Halo Gas and Galaxy Disk Kinematics Derived from Observations and  $\Lambda$ CDM Simulations of Mg II Absorption-selected Galaxies at Intermediate Redshift. *Astrophys. J.* **711**, 533–558 (2010). 0912.2746.
16. Rubin, K. H. R. *et al.* Low-ionization Line Emission from a Starburst Galaxy: A New Probe of a Galactic-scale Outflow. *Astrophys. J.* **728**, 55 (2011). 1008.3397.
17. Rubin, K. H. R. *et al.* Evidence for Ubiquitous Collimated Galactic-scale Outflows along the Star-forming Sequence at  $z \sim 0.5$ . *Astrophys. J.* **794**, 156 (2014). 1307.1476.
18. Nestor, D. B., Turnshek, D. A., Rao, S. M. & Quider, A. M. The Environments of Ultrastrong Mg II Absorbers. *Astrophys. J.* **658**, 185–202 (2007). astro-ph/0610760.
19. Prochter, G. E., Prochaska, J. X. & Burles, S. M. On the Incidence and Kinematics of Strong Mg II Absorbers. *Astrophys. J.* **639**, 766–780 (2006). astro-ph/0411776.
20. Gauthier, J.-R. Ultra-strong Mg II absorbers as a signature of cool intragroup gas. *Mon. Not. R. Astron. Soc.* **432**, 1444–1454 (2013). 1304.0006.

21. Péroux, C. *et al.* MUSE-ALMA haloes VII: survey science goals & design, data processing and final catalogues. *Mon. Not. R. Astron. Soc.* **516**, 5618–5636 (2022). 2211.16517.
22. Péroux, C. *et al.* Multiphase circumgalactic medium probed with MUSE and ALMA. *Mon. Not. R. Astron. Soc.* **485**, 1595–1613 (2019). 1901.05217.
23. Szakacs, R. *et al.* MUSE-ALMA haloes VI: coupling atomic, ionized, and molecular gas kinematics of galaxies. *Mon. Not. R. Astron. Soc.* **505**, 4746–4761 (2021). 2105.07280.
24. Weng, S. *et al.* MUSE-ALMA Haloes - VIII. Statistical study of circumgalactic medium gas. *Mon. Not. R. Astron. Soc.* **519**, 931–947 (2023). 2212.01395.
25. Zabl, J. *et al.* MusE GAs FLOW and Wind (MEGAFLOW) II. A study of gas accretion around  $z \approx 1$  star-forming galaxies with background quasars. *Mon. Not. R. Astron. Soc.* **485**, 1961–1980 (2019). 1901.11416.
26. Schroetter, I. *et al.* MusE GAs FLOW and Wind (MEGAFLOW) III: galactic wind properties using background quasars. *arXiv e-prints* (2019). 1907.09967.
27. Dutta, R. *et al.* Metal-enriched halo gas across galaxy overdensities over the last 10 billion years. *Mon. Not. R. Astron. Soc.* **508**, 4573–4599 (2021). 2109.10927.
28. Lofthouse, E. K. *et al.* MUSE Analysis of Gas around Galaxies (MAGG) - IV. The gaseous environment of  $z$  3–4 Ly  $\alpha$  emitting galaxies. *Mon. Not. R. Astron. Soc.* **518**, 305–331 (2023). 2209.15021.
29. Galbiati, M., Dutta, R., Fumagalli, M., Fossati, M. & Cantalupo, S. MUSE Analysis of Gas around Galaxies (MAGG) – VI. The cool and enriched gas environment of  $z$  *rsim*3 Ly $\alpha$  emitters. *arXiv e-prints* arXiv:2406.10350 (2024). 2406.10350.
30. Prochaska, J. X., Neeleman, M., Kanekar, N. & Rafelski, M. ALMA C II 158  $\mu$ m Imaging of an H I-selected Major Merger at  $z \sim 4$ . *Astrophys. J. Lett.* **886**, L35 (2019). 2005.10279.
31. Neeleman, M., Kanekar, N., Prochaska, J. X., Rafelski, M. A. & Carilli, C. L. [C II] 158  $\mu$ m Emission from  $z \sim 4$  H I Absorption-selected Galaxies. *Astrophys. J. Lett.* **870**, L19 (2019). 1812.06113.
32. Bordoloi, R. *et al.* EIGER IV: The cool 10<sup>4</sup>K circumgalactic environment of high- $z$  galaxies reveals remarkably efficient IGM enrichment. *arXiv e-prints* arXiv:2307.01273 (2023). 2307.01273.
33. Christensen, L. *et al.* Metal enrichment and evolution in four  $z > 6.5$  quasar sightlines observed with JWST/NIRSpec. *Astron. Astrophys.* **680**, A82 (2023). 2309.06470.
34. Neeleman, M., Prochaska, J. X., Kanekar, N. & Rafelski, M. A cold, massive, rotating disk galaxy 1.5 billion years after the Big Bang. *Nature* **581**, 269–272 (2020). 2005.09661.
35. van der Wel, A. *et al.* 3D-HST+CANDELS: The Evolution of the Galaxy Size-Mass Distribution since  $z = 3$ . *Astrophys. J.* **788**, 28 (2014). 1404.2844.
36. Matejek, M. S., Simcoe, R. A., Cooksey, K. L. & Seyffert, E. N. Mg II Absorption at  $2 < z < 6$  with Magellan/FIRE. II. A Longitudinal Study of H I, Metals, and Ionization in Galactic Halos. *Astrophys. J.* **764**, 9 (2013). 1207.2470.
37. Shen, Y. *et al.* Gemini GNIRS Near-infrared Spectroscopy of 50 Quasars at  $z \geq 5.7$ . *Astrophys. J.* **873**, 35 (2019). 1809.05584.
38. Bacon, R. *et al.* The MUSE Hubble Ultra Deep Field Survey. I. Survey description, data reduction, and source detection. *Astron. Astrophys.* **608**, A1 (2017). 1710.03002.
39. Weilbacher, P. M. *et al.* The data processing pipeline for the MUSE instrument. *Astron. Astrophys.* **641**, A28 (2020). 2006.08638.
40. Soto, K. T., Lilly, S. J., Bacon, R., Richard, J. & Conseil, S. ZAP - enhanced PCA sky subtraction for integral field spectroscopy. *Mon. Not. R. Astron. Soc.* **458**, 3210–3220 (2016). 1602.08037.
41. Wang, F. *et al.* A SPectroscopic Survey of Biased Halos in the Reionization Era (ASPIRE): JWST Reveals a Filamentary Structure around a  $z = 6.61$  Quasar. *Astrophys. J. Lett.* **951**, L4 (2023). 2304.09894.
42. Yang, J. *et al.* A SPectroscopic Survey of Biased Halos in the Reionization Era (ASPIRE): A First Look at the Rest-frame Optical Spectra of  $z > 6.5$  Quasars Using JWST. *Astrophys. J. Lett.* **951**, L5 (2023). 2304.09888.

43. Sun, F. *et al.* First Peek with JWST/NIRCam Wide-field Slitless Spectroscopy: Serendipitous Discovery of a Strong [O III]/H $\alpha$  Emitter at  $z = 6.11$ . *Astrophys. J. Lett.* **936**, L8 (2022). 2207.11259.
44. Sun, F. *et al.* A SPectroscopic survey of biased halos In the Reionization Era (ASPIRE): Spectroscopically Complete Census of Obscured Cosmic Star Formation Rate Density at  $z = 4 - 6$ . *arXiv e-prints* arXiv:2412.06894 (2024). 2412.06894.
45. Urrutia, T. *et al.* The MUSE-Wide Survey: survey description and first data release. *Astron. Astrophys.* **624**, A141 (2019). 1811.06549.
46. Bertin, E. & Arnouts, S. SExtractor: Software for source extraction. *Astron. Astrophys. Suppl.* **117**, 393–404 (1996).
47. Krogager, J.-K. VoigtFit: A Python package for Voigt profile fitting. *arXiv e-prints* (2018). 1803.01187.
48. Schaerer, D. The transition from Population III to normal galaxies: Ly $\alpha$  and He II emission and the ionising properties of high redshift starburst galaxies. *Astron. Astrophys.* **397**, 527–538 (2003). astro-ph/0210462.
49. Kennicutt, J., Robert C. The Global Schmidt Law in Star-forming Galaxies. *Astrophys. J.* **498**, 541–552 (1998). astro-ph/9712213.
50. Osterbrock, D. E. & Ferland, G. J. *Astrophysics of gaseous nebulae and active galactic nuclei* (2006).
51. Sobral, D. & Matthee, J. Predicting Ly $\alpha$  escape fractions with a simple observable. Ly $\alpha$  in emission as an empirically calibrated star formation rate indicator. *Astron. Astrophys.* **623**, A157 (2019). 1803.08923.
52. Krogager, J.-K., Møller, P., Fynbo, J. P. U. & Noterdaeme, P. Consensus report on 25 yr of searches for damped Ly  $\alpha$  galaxies in emission: confirming their metallicity-luminosity relation at  $z \text{ geq } 2$ . *Mon. Not. R. Astron. Soc.* **469**, 2959–2981 (2017). 1704.08075.
53. Krogager, J.-K. *et al.* The High  $A_V$  Quasar Survey: Reddened Quasi-Stellar Objects Selected from Optical/Near-Infrared Photometry II. *Astrophys. J. Suppl. Ser.* **217**, 5 (2015). 1410.7783.
54. Hashimoto, T. *et al.* The MUSE Hubble Ultra Deep Field Survey. X. Ly $\alpha$  equivalent widths at  $2.9 < z < 6.6$ . *Astron. Astrophys.* **608**, A10 (2017). 1711.01747.
55. Wisotzki, L. *et al.* Extended Lyman  $\alpha$  haloes around individual high-redshift galaxies revealed by MUSE. *Astron. Astrophys.* **587**, A98 (2016). 1509.05143.
56. Witstok, J. *et al.* Inside the bubble: exploring the environments of reionisation-era Lyman- $\alpha$  emitting galaxies with JADES and FRESCO. *Astron. Astrophys.* **682**, A40 (2024). 2306.04627.
57. Drake, A. B. *et al.* The MUSE Hubble Ultra Deep Field Survey. VI. The faint-end of the Ly $\alpha$  luminosity function at  $2.91 < z < 6.64$  and implications for reionisation. *Astron. Astrophys.* **608**, A6 (2017). 1711.03095.
58. Heintz, K. E. *et al.* The JWST-PRIMAL Legacy Survey. A JWST/NIRSpec reference sample for the physical properties and Lyman- $\alpha$  absorption and emission of  $\sim 500$  galaxies at  $z = 5.5 - 13.4$ . *arXiv e-prints* arXiv:2404.02211 (2024). 2404.02211.
59. Ferland, G. J. *et al.* The 2017 Release Cloudy. *Rev. Mexicana Astron. Astrofis.* **53**, 385–438 (2017). 1705.10877.
60. Rafelski, M., Wolfe, A. M., Prochaska, J. X., Neeleman, M. & Mendez, A. J. Metallicity Evolution of Damped Ly $\alpha$  Systems Out to  $z \sim 5$ . *Astrophys. J.* **755**, 89 (2012). 1205.5047.
61. Jenkins, E. B., Savage, B. D. & Spitzer, L., Jr. Abundances of interstellar atoms from ultraviolet absorption lines. *Astrophys. J.* **301**, 355–379 (1986).
62. Greene, T. P. *et al.*  $\lambda = 2.4$  to  $5 \mu\text{m}$  spectroscopy with the James Webb Space Telescope NIRCam instrument. *Journal of Astronomical Telescopes, Instruments, and Systems* **3**, 035001 (2017).
63. Murphy, E. J. *et al.* Calibrating Extinction-free Star Formation Rate Diagnostics with 33 GHz Free-free Emission in NGC 6946. *Astrophys. J.* **737**, 67 (2011). 1105.4877.
64. Neeleman, M. *et al.* Molecular Emission from a Galaxy Associated with a  $z \sim 2.2$  Damped Ly $\alpha$  Absorber. *Astrophys. J. Lett.* **856**, L12 (2018). 1803.05914.

65. Neeleman, M. *et al.* [C II] 158- $\mu\text{m}$  emission from the host galaxies of damped Lyman-alpha systems. *Science* **355**, 1285–1288 (2017). 1703.07797.
66. Carnall, A. C., McLure, R. J., Dunlop, J. S. & Davé, R. Inferring the star formation histories of massive quiescent galaxies with BAGPIPES: evidence for multiple quenching mechanisms. *Mon. Not. R. Astron. Soc.* **480**, 4379–4401 (2018). 1712.04452.
67. Calzetti, D. *et al.* The Dust Content and Opacity of Actively Star-forming Galaxies. *Astrophys. J.* **533**, 682–695 (2000). astro-ph/9911459.
68. Peng, C. Y., Ho, L. C., Impey, C. D. & Rix, H.-W. Detailed Structural Decomposition of Galaxy Images. *Astron. J.* **124**, 266–293 (2002). astro-ph/0204182.
69. Peng, C. Y., Ho, L. C., Impey, C. D. & Rix, H.-W. Detailed Decomposition of Galaxy Images. II. Beyond Axisymmetric Models. *Astron. J.* **139**, 2097–2129 (2010). 0912.0731.
70. Sun, W. *et al.* The Structure and Morphology of Galaxies during the Epoch of Reionization Revealed by JWST. *Astrophys. J.* **960**, 104 (2024). 2308.09076.
71. Li, Z. *et al.* MAGNIF: A Tentative Lensed Rotating Disk at  $z = 8.34$  detected by JWST NIRCam WFSS with Dynamical Forward Modeling. *arXiv e-prints* arXiv:2310.09327 (2023). 2310.09327.
72. Nelson, E. J. *et al.* FRESCO: An extended, massive, rapidly rotating galaxy at  $z=5.3$ . *arXiv e-prints* arXiv:2310.06887 (2023). 2310.06887.
73. Outini, M. & Copin, Y. Forward modeling of galaxy kinematics in slitless spectroscopy. *Astron. Astrophys.* **633**, A43 (2020). 1910.07803.
74. Liang, J. *et al.* Connection between galaxy morphology and dark-matter halo structure I: a running threshold for thin discs and size predictors from the dark sector. *arXiv e-prints* arXiv:2403.14749 (2024). 2403.14749.
75. Nelson, D. *et al.* First results from the IllustrisTNG simulations: the galaxy colour bimodality. *Mon. Not. R. Astron. Soc.* **475**, 624–647 (2018). 1707.03395.
76. Gnedin, N. Y. & Kravtsov, A. V. Environmental Dependence of the Kennicutt-Schmidt Relation in Galaxies. *Astrophys. J.* **728**, 88 (2011). 1004.0003.
77. Dekel, A. & Birnboim, Y. Galaxy bimodality due to cold flows and shock heating. *Mon. Not. R. Astron. Soc.* **368**, 2–20 (2006). astro-ph/0412300.
78. Dekel, A. *et al.* A mass threshold for galactic gas discs by spin flips. *Mon. Not. R. Astron. Soc.* **493**, 4126–4142 (2020). 1912.08213.
79. Girelli, G. *et al.* The stellar-to-halo mass relation over the past 12 Gyr. I. Standard  $\Lambda$ CDM model. *Astron. Astrophys.* **634**, A135 (2020). 2001.02230.

Table 1: Galaxy property measurements around the US-MGII absorbers

<b>J1306+0356 LAE1</b>	
$z_{em}$	4.867
R.A.	13:06:09.53
Dec.	+03:55:58.08
$D$ (kpc)	201
$f_{Ly\alpha}$ ( $10^{-17}$ erg s $^{-1}$ cm $^{-2}$ )	$2.45 \pm 0.81$
EW ( $\text{\AA}$ )	$73.15 \pm 24.05$
FWHM (km s $^{-1}$ )	121
SFR ( $M_{\odot}$ yr $^{-1}$ )	$5.75 \pm 1.89$
<b>J1306+0356 LAE2</b>	
$z_{em}$	4.865
R.A.	13:06:07.49
Dec.	+03:56:53.88
$D$ (kpc)	197
$f_{Ly\alpha}$ ( $10^{-17}$ erg s $^{-1}$ cm $^{-2}$ )	$0.67 \pm 0.31$
EW ( $\text{\AA}$ )	$20.01 \pm 9.37$
<b>J0305M3150-HeI-2708</b>	
$z_{em}$	2.564
R.A.	03:05:17.11
Dec.	-31:50:52.08
$D$ (kpc)	38
$f_{He\ \lambda 10830}$ ( $10^{-17}$ erg s $^{-1}$ cm $^{-2}$ )	$1.37 \pm 0.42$
FWHM (km s $^{-1}$ )	710
$f_{[S\ III]\lambda 9531}$ ( $10^{-17}$ erg s $^{-1}$ cm $^{-2}$ )	$1.22 \pm 0.52$
$f_{[S\ III]\lambda 9067}$ ( $10^{-17}$ erg s $^{-1}$ cm $^{-2}$ )	$1.01 \pm 0.49$
$f_{Pa\gamma}$ ( $10^{-17}$ erg s $^{-1}$ cm $^{-2}$ )	$1.07 \pm 0.38$
$f_{Pa10}$ ( $10^{-17}$ erg s $^{-1}$ cm $^{-2}$ )	$0.89 \pm 0.43$
EW <sub>He <math>\lambda</math> 10830</sub> ( $\text{\AA}$ )	$329.51 \pm 51.0$
EW <sub>[S III]<math>\lambda</math> 9531</sub> ( $\text{\AA}$ )	$275.31 \pm 66.16$
EW <sub>Pa<math>\gamma</math></sub> ( $\text{\AA}$ )	$124.19 \pm 44.11$
$S_{cont}$ (mJy)	$424 \pm 110$
$L_{FIR}$ (erg s $^{-1}$ )	$(5.74 \pm 1.58) \times 10^{11}$
$\log M_{*}/M_{\odot}$	$10.73^{+0.02}_{-0.60}$
$\log M_{dust}/M_{\odot}$	$8.30 \pm 0.11$
SFR ( $M_{\odot}$ yr $^{-1}$ )	$121 \pm 33$

## Extended Data

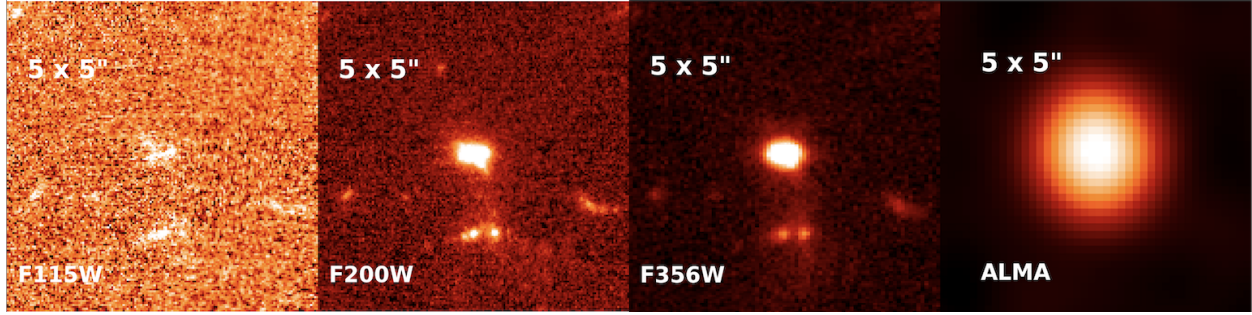


Figure 1: The JWST/NIRCam imaging of J0305M31-He1-2708 in the F115W, F200W, and F356W bands. The last panel shows the ALMA tapered imaging to increase the SNR. All images are  $5 \times 5''$  in size.

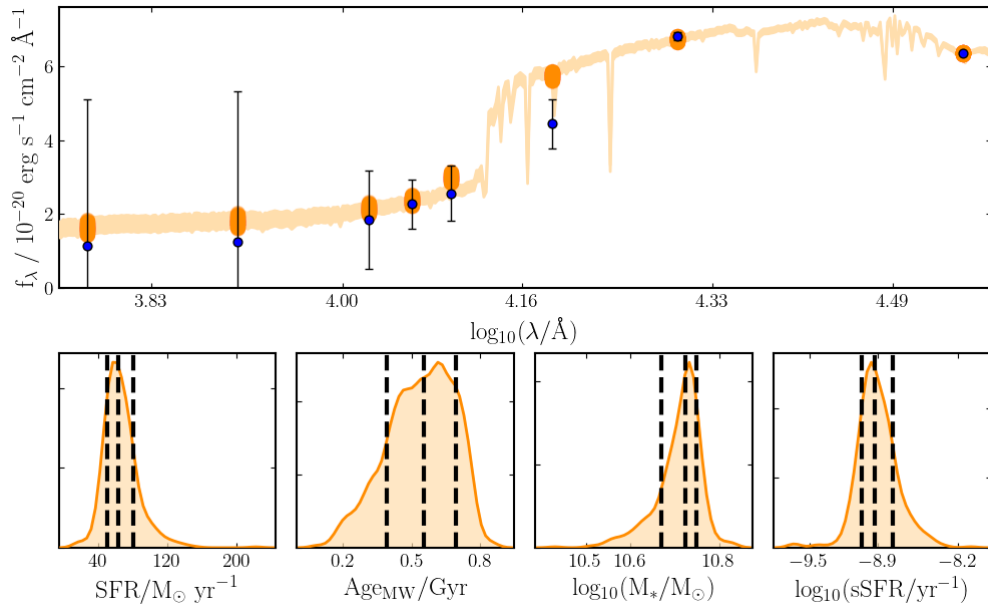


Figure 2: Spectral energy distributions fitting of J0305M31-He1-2708 using BAGPIPES. We use photometry from JWST NIRCam F115W, F200W, F356W bands, and HST F105W, F125W, F160W, F606W, and F814W bands.

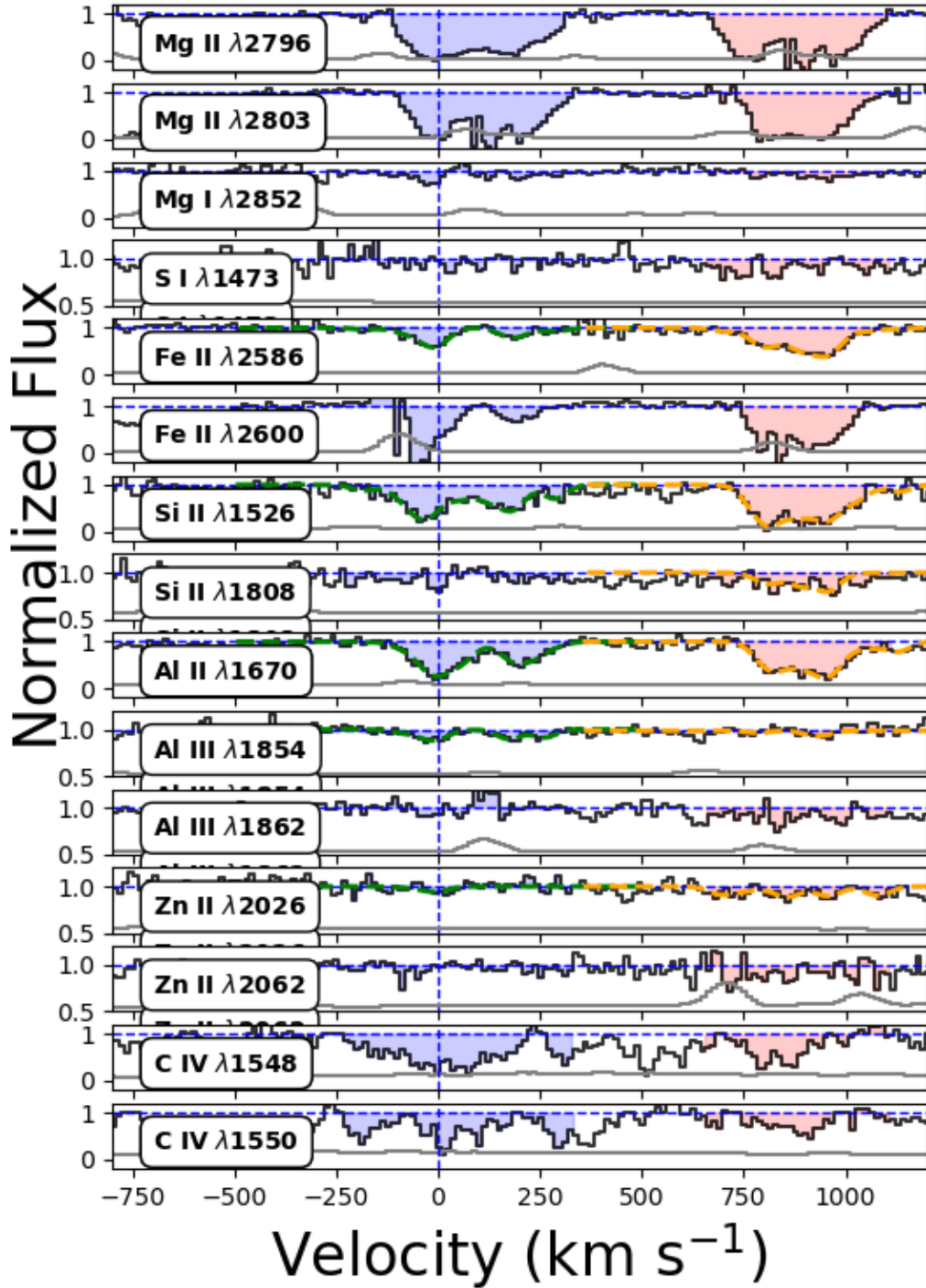


Figure 3: Complete velocity profile of absorption lines of the two USMGII structures towards J1306+3150 at  $z = 4.87$ . System 1 at  $z = 4.8634$  and system 2 at  $z = 4.8821$  are plotted in blue and red shadow, respectively. The Voigt fitting profiles of Fe II, Si II, Al II, Al III, and Zn II lines in these two systems are plotted with green and orange dashed lines, respectively. The quasar spectra were taken with Magellan/FIRE with a spectral resolution of  $R \sim 6000$ .

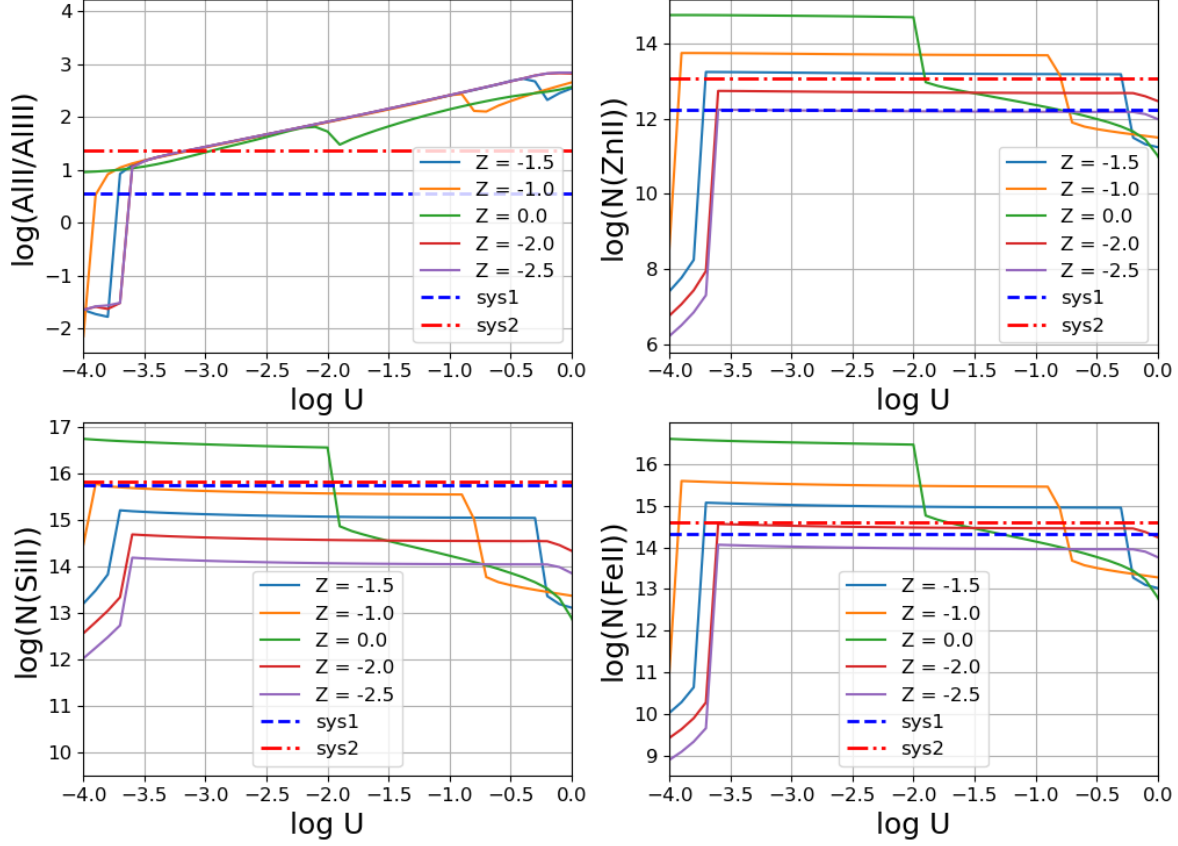


Figure 4: CLOUDY modeling of two absorbing systems at  $z \sim 4.9$  along the sightline J1306+3150. The observed values of system 1 at  $z = 4.8634$  and system 2 at  $z = 4.8821$  are plotted as blue dashed and red dash-dotted lines, respectively. The modeling curves are plotted with different metallicities ( $\log(Z/Z_{\odot})$ ) ranging from  $-2.5$  to  $0$ . From the upper left to the lower right, we plot the column density ratio of Al II to Al III against ionization parameter, and the column densities of Zn II, Si II, and Fe II against ionization parameter, respectively.

Extended Data Table 1: Quasar and absorber information in this work. We list the targets that have MUSE data. We remeasure the absorber rest-frame equivalent width and velocity width for the systems towards J0305–3150 and J1306+0356. Other values are presented in Chen et al.,(2017)<sup>3</sup>.

QSO	RA	DEC	$z_{\text{abs}}$	EW (Å)	$\Delta v$ km s <sup>-1</sup>	Exposure Time (hours)	PI & Project ID
<b>J0305–3150</b>	03:05:16.9	-31:50:55.98	2.5652	2.869±0.481	524.6	2.5	Venemans 094.B-0893
J0836+0054	08:36:43.9	+00:54:53.3	3.7443	2.509±0.016	510.4	5.3	Bian 106.210Z
<b>J1306+0356<sub>a</sub></b>	13:06:08.3	+03:56:26.3	4.8634	2.891±0.109	541.5	10.4	Ellis 0103.A-0140
<b>J1306+0356<sub>b</sub></b>	13:06:08.3	+03:56:26.3	4.8821	< 2.949	465.9	10.4	Ellis 0103.A-0140
J1509-1749	15:09:41.78	-17:49:26.80	3.3925	5.679±0.056	811.5	1.0	Farina 0101.A-0656
J2211-3206	22:11:12.39	-32:06:12.95	3.7144	3.505±0.068	623.4	1.0	Farina 0101.A-0656
J1030+0525	10:30:27.09	+05:24:55.02	2.78	2.617±0.069	583.9	1.0	Karman 095.A-0714

Extended Data Table 2: Re-measurements of the ion equivalent widths (EW) of J1306+1356 are presented. We denote the system at  $z = 4.8634$  as system 1 and the one at  $z = 4.8821$  as system 2. The blended region refers to Mg II( $\lambda 2803$ ) in system 1, which is blended with Mg II( $\lambda 2796$ ) in system 2. Columns 4 and 5 show the Voigt-profile fitted column densities of ions with a Doppler parameter  $b = 25 \text{ km s}^{-1}$ . The uncertainties are given by varying the  $b$  value by  $\pm 5 \text{ km s}^{-1}$ . We do not measure the column densities of Mg II and C IV lines due to strong blending in these two systems.

Ions	EW(System 1) ( $\text{\AA}$ )	EW(System 2) ( $\text{\AA}$ )	log N (System1) ( $\text{cm}^{-2}$ )	log N (System2) ( $\text{cm}^{-2}$ )
Mg II( $\lambda 2796$ )	$>2.920 \pm 0.120$	-	-	-
Mg II blended	$2.959 \pm 0.160$	-	-	-
Mg II( $\lambda 2803$ )	-	$2.371 \pm 0.097$	-	-
Mg II( $\lambda 2852$ )	$0.391 \pm 0.250$	$0.359 \pm 0.181$	$< 13.98$	$< 13.94$
Fe II( $\lambda 2586$ )	$0.553 \pm 0.141$	$1.141 \pm 0.123$	$14.32 \pm 0.02$	$14.60 \pm 0.12$
Si II( $\lambda 1526$ )	$0.915 \pm 0.062$	$1.137 \pm 0.060$	$15.76 \pm 0.03$	$15.82 \pm 0.05$
Al II( $\lambda 1670$ )	$0.923 \pm 0.069$	$0.988 \pm 0.067$	$13.59 \pm 0.11$	$13.726 \pm 0.10$
Al III( $\lambda 1854$ )	$0.165 \pm 0.108$	$0.106 \pm 0.105$	$13.034 \pm 0.01$	$13.649 \pm 0.11$
Zn II( $\lambda 2026$ )	$< 0.027$	$0.160 \pm 0.092$	$< 12.237$	$13.056 \pm 0.05$
C IV( $\lambda 1548$ )	$1.141 \pm 0.298$	$0.552 \pm 0.267$	-	-
C IV( $\lambda 1550$ )	$0.791 \pm 0.358$	$0.435 \pm 0.251$	-	-